PFC/JA-84-26

Observation of Parametric Instabilities in the Lower Hybrid Range of Frequencies in the Alcator C Tokamak

Y. Takase, M. Porkolab, J. J. Schuss
R. L. Watterson, C. L. Fiore

Plasma Fusion Center
Massachusetts Institute of Technology
Cambridge, MA 02139

July 1984

This work was supported by the U.S. Department of Energy Contract No. DE-AC02-78ET51013. Reproduction, translation, publication, use and disposal, in whole or in part by or for the United States government is permitted.

Observation of parametric instabilities in the lower hybrid range of frequencies in the Alcator C tokamak

Y. Takase, M. Porkolab, J. J. Schuss,[a)] R. L. Watterson, and C. L. Fiore

Plasma Fusion Center, Massachusetts Institute of Technology, Cambridge, Massachusetts 02139

(Received

Parametric decay processes have been studied using rf probes and CO_2 laser scattering during the lower-hybrid wave heating and current drive experiments in the Alcator C tokamak. The most important process is believed to be the nonresonant decay into ion-cyclotron quasimodes and/or that into electron-Landau quasimodes. At lower densities $\omega_0/\omega_{LH}(0) > 2$ [where ω_0 is the frequency of the injected pump wave and $\omega_{LH}(0)$ is the lower-hybrid frequency evaluated at the plasma center], where efficient current drive and electron heating are obtained, parametric decay is absent or very weak. At higher densities [$\omega_0/\omega_{LH}(0) \lesssim 2$] strong parametric decay is observed which correlates well with ion tail formation near the plasma edge. At these high densities no significant heating or current drive have been observed. Parametric decay may be, at least partially, responsible for loss of wave power near the plasma periphery.

PACS numbers: 52.35.Mw, 52.35.Py, 52.50.Gj, 52.40.Db

I. INTRODUCTION

Most lower-hybrid wave heating and current drive experiments suffer degradation of efficiency at high plasma densities such that $\omega_0/\omega_{LH}(0) \lesssim 2$.[1] At such densities parametric decay is often observed and may be partially responsible for the deterioration of efficiencies. Here, we present experimental results on parametric decay processes obtained by rf probes and CO_2 laser scattering during the Alcator C lower-hybrid experiments.[2] Strong parametric decay is observed for line-average densities $\overline{n}_e \gtrsim 1.5\times10^{14}\,\mathrm{cm}^{-3}$ in hydrogen [corresponding to $\omega_0/\omega_{LH}(0) \lesssim 1.8$], and for $\overline{n}_e \gtrsim 2.0\times10^{14}\,\mathrm{cm}^{-3}$ in deuterium [corresponding to $\omega_0/\omega_{LH}(0) \lesssim 2.2$]. The excitation of parametric decay correlated well with the formation of ion tail near the plasma surface.[3,4] Above these critical densities no significant heating or current drive have been observed. In this paper, we also compare these experimental observations with the theory of parametric decay instabilities.[5-10] The understanding of parametric processes is important in applying lower-hybrid heating and current drive to high density plasmas, where $\omega_0/\omega_{LH}(0) \lesssim 2$.

The plan of the paper is as follows: In Sec. II, theoretical estimates of growth rates and thresholds are presented. In Sec. III, the results of rf probe measurements are presented and correlated with the formation of ion tail observed by the charge exchange analyzer. In Sec. IV, the CO_2 laser scattering data will be presented and compared with the rf probe data. Interpretation of the experimental results are also presented. Finally, in Sec. V the summary and conclusions are given.

II. THEORETICAL ESTIMATES OF GROWTH RATES AND THRESHOLDS

A. Homogeneous Plasma Growth Rates

The parametric dispersion relation [Eq. (1) of Ref. 10] was solved numerically using the same method as described in Ref. 10. Decay into ion-cyclotron quasimodes ($\omega \simeq n\omega_{ci}$) and decay into nonresonant (electron-Landau) quasimodes ($\omega \simeq k_{||}v_{te}$)[5,6] were studied in detail. Decay into ion-sound (or ion-Landau) quasimodes ($\omega \simeq k_{||}v_{ti}$) was discussed previously.[10] Here, ω and $k_{||}$ correspond to the frequency and the parallel (to the equilibrium magnetic field) wave number of the low-frequency quasimode, ω_{ci} is the ion-cyclotron frequency, n is an integer, and $v_{te,i} \equiv (2T_{e,i}/m_{e,i})^{1/2}$ are the electron and ion thermal speeds. First, we assume that the plasma is homogeneous in space. No convective losses are considered in this sub-section. In this case the growth rate is maximized when $\theta = \pi/2$, where θ is the angle between $\mathbf{k}_{0\perp}$ and $\mathbf{k}_{\perp}^{-}$. The subscript '0' refers to the pump wave whereas the superscript '$-$' refers to the lower sideband wave ($\omega^{-} \equiv \omega - \omega_0$, $\mathbf{k}^{-} \equiv \mathbf{k} - \mathbf{k}_0$). In this sub-section we shall take $\theta = \pi/2$. The local electric field is calculated by WKB techniques, assuming resonance cone propagation (see Ref. 10). The calculated electric field is expected to be close to the real electric field near the waveguide mouth, but would start to deviate significantly as the waves propagate further into the plasma (due to spatial broadening of resonance cones).

In Fig. 1 we show a solution of the parametric dispersion relation for a deuterium plasma, with $B = 6.7\,\mathrm{T}$ ($B = 8\,\mathrm{T}$ at the plasma center), $n_e = 1.9 \times 10^{14}\,\mathrm{cm}^{-3}$, $T_e = T_i = 250\,\mathrm{eV}$, which were typical parameters for Alcator C near $r/a \simeq 3/4$ where the CO_2 scattering data were obtained. We have taken $P_{\mathrm{rf}} = 100\,\mathrm{kW}$, $ck_{0||}/\omega_0 = 3$, and $ck_{||}^{-}/\omega_0 = 7$. In Fig. 1(a) the growth rate γ and

the real part of the frequency ω_R of the quasimode ($\omega \equiv \omega_R + i\gamma$) are plotted as functions of the wave number k of the quasimode, and in Fig. 1(b) γ is plotted as a function of ω_R. The first few ion-cyclotron harmonics are ion-cyclotron quasimodes ($|\epsilon_R| \gg 1$, $|\chi_{iI}| \gg |\chi_{eI}|$) whereas the peak in the growth rate near $\omega/\omega_0 \simeq 0.15$ is due to decay into nonresonant quasimode which is driven by both electron Landau damping and ion-cyclotron damping ($|\epsilon_R| \gg 1$, $|\chi_{iI}| \simeq |\chi_{eI}|$). Here, $\epsilon(\mathbf{k},\omega) = 1 + \chi_e(\mathbf{k},\omega) + \chi_i(\mathbf{k},\omega)$ is the dielectric function, χ_e and χ_i are the electron and ion components of the susceptibility, and subscripts 'R' and 'I' refer to the real and imaginary parts, respectively. The transition from decay into ion-cyclotron quasimodes to decay into nonresonant quasimode is smooth and continuous. There is a small peak below the ion-cyclotron frequency which corresponds to the ion-sound quasimode discussed in Ref. 10.

In contrast to the case of decay into ion-sound quasimodes, it is not easy to obtain a simplified analytical solution for the growth rate and threshold since different parts of the susceptibilities are usually of the same order of magnitude. However, scaling of the growth rate and the frequency can be studied by numerically solving the parametric dispersion relation. First, in Fig. 2 we show the dependence of the growth rate on density. The maximum growth rate among all ion-cyclotron harmonics, $\gamma_{\max}$, and the real part of the frequency corresponding to the maximum growth rate, $\omega_{R\max}$, are plotted as functions of the local electron density. The growth rate increases rapidly as the density approaches the mode conversion density, whereas the real part of the frequency changes very little. On the other hand, $\omega_{R\max}$ varies linearly with v_{te} or as $\sqrt{T_e}$ when the electron temperature is varied ($\omega_{R\max} \simeq 0.4 k_{\|} v_{te}$ with discrete jumps between ion-cyclotron harmonics) as shown in Fig. 3. This scaling of $\omega_{R\max}$ with $k_{\|}v_{te}$ still holds when $k_{\|}$ is varied with T_e held fixed as shown in Fig. 4. The maximum growth rate $\gamma_{\max}$ also increases with

$k_{||}$. However, $\gamma_{\max}$ starts to turn over when $k_{||}$ becomes so high that electron Landau damping at the lower sideband becomes appreciable. Consequently, there is a maximum in $\gamma_{\max}$ at around $|\omega^-/k_{||}^- v_{te}| \simeq 4$.

In Fig. 5 we show the dependences of $\gamma_{\max}$ and $\omega_{R\max}$ as functions of the major radial distance from the plasma center, $x \equiv R - R_0$, for typical Alcator C parameters. In particular, in this figure we considered deuterium plasma with the parameters $B = 8\,\mathrm{T}$, $\bar{n}_e = 2.1 \times 10^{14}\,\mathrm{cm}^{-3}$, $T_{e0} = 1.5\,\mathrm{keV}$, $P_{\mathrm{rf}} = 100\,\mathrm{kW}$, $ck_{0||}/\omega_0 = 3$, and $ck_{||}^-/\omega_0 = 7$. The density profile for $r \leq a = 16.5\,\mathrm{cm}$ was assumed to be $n_e = n_{e0}[1-(r/a_n)^2]^{1/2}$,[11] where $a_n = 17.5\,\mathrm{cm}$, and for $r > a$ it was assumed to fall off exponentially to $n_e = 5 \times 10^{12}\,\mathrm{cm}^{-3}$ at $r = r_{\mathrm{wg}} = 18\,\mathrm{cm}$ where the waveguide array (grill) is located. The electron temperature profile for $r < a$ was assumed to be $T_e = T_{e0}\exp[-(r/a_T)^2]$,[11] where $a_T = 9\,\mathrm{cm}$, and was assumed to fall off from $20\,\mathrm{eV}$ at $r = a$ to $5\,\mathrm{eV}$ at $r = r_{\mathrm{wg}}$. In the region plotted $T_i = T_e$ was assumed. Two curves for the growth rate γ are shown. The triangles are for the case $\theta = \pi/2$ (*i.e.*, $\mathbf{k}_{0\perp} \perp \mathbf{k}_{\perp}^-$). The coupling is dominated by the $\mathbf{E} \times \mathbf{B}$ coupling term for this case. The crosses represent the case $\theta = 0$ (*i.e.*, $\mathbf{k}_{0\perp} \parallel \mathbf{k}_{\perp}^-$) when the $E_{||}$ coupling dominates. The latter case is relevant when considering the convective threshold near the plasma edge. The maximum in the growth rate occurs near the limiter radius for the $\mathbf{E} \times \mathbf{B}$ coupling case whereas for the $E_{||}$ coupling case γ is finite and positive only near the plasma edge ($r/a \gtrsim 1$ for the present case).

The growth rate does not follow a simple power law when the rf power is varied. From Fig. 6 it is clear that while at medium power levels ($10 \lesssim P_{\mathrm{rf}} \lesssim 100\,\mathrm{kW}$) $\gamma \propto P_{\mathrm{rf}}^{0.75}$, at higher power levels ($P_{\mathrm{rf}} \gtrsim 100\,\mathrm{kW}$) the growth rate increases less rapidly with rf power, namely $\gamma \propto P_{\mathrm{rf}}^{0.6}$. (Near the waveguide mouth where $n_e \simeq 5 \times 10^{12}\,\mathrm{cm}^{-3}$, the $E_{||}$ coupling dominates and $\gamma \propto P_{\mathrm{rf}}^{0.5}$.) This behavior should be taken into account when estimating the convective threshold using the

homogeneous growth rate. Finally, we note that the homogeneous plasma threshold power in the present case is at $P_{\rm rf} \simeq 1\,{\rm kW}$, and is due to collisional damping of the sideband cold lower-hybrid wave.

B. Convective Effects

In general, thresholds of parametric instabilities are significantly increased over the homogeneous plasma values when convective effects are taken into account. The usual way to estimate convective thresholds is to assume resonance cone propagation for the pump lower-hybrid wave.[6,7] However, finite k_θ (poloidal wave number) spectrum, electromagnetic effects (which become important for $|n_\parallel| \lesssim 2$), and scattering[12-14] from experimentally observed large-amplitude low-frequency ($\omega_l \ll \gamma$, $\omega_l \ll \omega_R \sim \omega_{ci}$) density fluctuations[15] all tend to distort the resonance cone structure. These phenomena produce two competing effects: convective losses are reduced, but at the same time the pump wave amplitude and the growth rate are also reduced. Another extreme is to assume that the pump wave fills the entire flux surface more or less uniformly. For this case we recover the homogeneous plasma threshold, modified by mismatch effects due to density and temperature gradients.[6,16] However, the local electric field for a given input rf power is significantly reduced from the case where the resonance cones exist since rf power has to spread over a larger surface area. The experimental situation should be somewhere between these two extremes. Near the waveguide mouth we expect strong resonance cone pattern; however, as the wave propagates farther into the plasma the distortion of the resonance cones become progressively more severe, and eventually the resonance cones should be completely destroyed after several toroidal transits. This picture is supported by CO_2 laser scattering data, at least at relatively high densities where parametric decay is observed.[17] A quantitative prediction of the

threshold for this case is rather difficult since one has to follow the decay wave along its trajectory until enough [usually taken to be $\exp(2\pi)$] amplification of the decay wave power is obtained. This condition is given by

$$\int_0^{\varsigma} \frac{\gamma(\varsigma)}{|v_{2\varsigma}|} d\varsigma = \pi,$$

where ς is the coordinate along the trajectory of the decay wave and $v_{2\varsigma}$ is the component of the decay wave group velocity along the trajectory. In addition to changing plasma parameters, along the ray trajectory the pump electric field is varying because of resonance cone spreading. A better estimate could be made with the aid of a ray tracing code which includes the effects of scattering by density fluctuations.[13] Below, we shall give some representative examples of the threshold rf power by assuming a homogeneous plasma but different spatial distributions of the pump wave. In reality, the decay wave will not stay at the radial location where the growth rate is maximum, but will propagate to regions of different plasma parameters and lower growth rate, which contributes to raising the threshold above the value calculated here.[10]

First, we consider the case with undistorted resonance cones. There is an optimum angle of propagation θ that $\mathbf{k}_{\perp}^{-}$ makes with $\mathbf{k}_{0\perp}$. This is determined by the competition between increasing the parametric coupling constant μ and reducing the convective loss. We shall use the coupling constant given by μ^{-} in Eq. (5) of Ref. 10, namely

$$\mu \simeq \frac{e}{m_e} \frac{k}{k^{-}} \left[\left(\frac{k_{\parallel}^{-} E_{0\parallel}^2}{\omega_0^2} \right)^2 + \left(\frac{k_{\perp}^{-} E_{0\perp} \sin\theta}{\omega_0 \omega_{ce}} \right)^2 \right]^{1/2} .$$

Two important contributions to the parametric coupling constant are that due to the $\mathbf{E} \times \mathbf{B}$ motion of the electrons (the second term, which varies as $\sin\theta$) and

that due to the parallel motion of the electrons driven by $E_{||}$ (the first term, which is independent of θ and dominates for small angles,[6] $\sin\theta < \omega_{pe}^2/\omega_0\omega_{ce}$). The polarization drift term (which varies as $\cos\theta$) is smaller than the parallel term by at least a factor of $\omega_{pe}^2/\omega_{ce}^2$. Near the plasma edge we find that the convective growth factor maximizes when $\theta = 0$ so that the decay wave can travel nearly parallel to the pump wave. The coupling for this case is due to $E_{||}$. This is true even at $r \simeq a$ where $\mathbf{E} \times \mathbf{B}$ coupling dominates over the $E_{||}$ coupling in a homogeneous plasma (see Fig. 5). (The optimum angle becomes finite at higher densities.) We shall take representative parameters of deuterium plasma, $B = 6.2\,\mathrm{T}$, $n_e = 5 \times 10^{12}\,\mathrm{cm}^{-3}$, $T_e = T_i = 5\,\mathrm{eV}$, $ck_{0||}/\omega_0 = 3$, and $ck_{||}^-/\omega_0 = 7$, corresponding to the values near the waveguide mouth in Alcator C where the $E_{||}$ coupling term is large. The homogeneous plasma threshold under these conditions is $P_{\mathrm{rf}} \simeq 5\,\mathrm{kW}$. The convective threshold for this case is $P_{\mathrm{rf}} \simeq 50\,\mathrm{kW}$. However, we note that the distance required for the decay wave power to amplify by $\exp(2\pi)$ is approximately 4 m, which is roughly one complete toroidal revolution. Account must also be taken of the decreasing $E_{||}$ driven growth rate as the wave propagate into the plasma (see Fig. 5). This will further raise the threshold. In order for the decay wave to have amplified by $\exp(2\pi)$ by the time it has traveled 60° in the toroidal direction (where the CO_2 laser scattering data were obtained) a growth rate of $\gamma/\omega_0 = 0.007$ is required which corresponds to an rf power of nearly 2 MW.

In the second limit, if we assume that the pump wave spreads over the entire flux surface uniformly, the pump wave electric field is reduced by a factor $[(2\pi^2 Ra^2)/(2L_yL_z)]^{1/2}$ from the case of resonance cone propagation. Here, $2\pi^2 Ra^2$ is the surface area of the flux surface at $r = a$, and $2L_yL_z$ is the cross-sectional area of the two resonance cones (where L_y and L_z are the dimensions of the waveguide array in the poloidal and toroidal directions, respectively). We shall take repre-

sentative edge parameters of deuterium plasma, $B = 6.4\,\mathrm{T}$, $n_e = 0.9 \times 10^{14}\,\mathrm{cm}^{-3}$, $T_e = T_i = 20\,\mathrm{eV}$, $ck_{0\|}/\omega_0 = 3$, and $ck_{\|}^{-}/\omega_0 = 7$, corresponding to the peak of the growth rate in Fig. 5. The homogeneous plasma threshold under these conditions is $P_{\mathrm{rf}} \simeq 1\,\mathrm{kW}$. The threshold rf power for this case is 2MW. This model is not supported by the CO_2 laser scattering data. At 60° away toroidally from the wave launcher during its first pass, the pump wave appears to be still fairly well localized.[17]

III. RF PROBE MEASUREMENTS

Externally launched lower-hybrid pump wave, as well as parametrically excited lower- and upper-sideband lower-hybrid waves and low-frequency quasimodes were studied with rf probes during the lower-hybrid heating and current drive experiments on the Alcator C tokamak. A relative phasing between adjacent waveguides of $\Delta\phi = 180^{\circ}$ was used for most of our data. The triaxial rf probe had a floating sheath, and the Molybdenum probe tip was 1 mm long and 0.4 mm in diameter. The rf probes were also used as Langmuir probes to study edge plasma parameters and density fluctuations. Several rf probes located at different toroidal and poloidal locations were used (see Fig. 7). Also shown are the locations of the two 4×4 waveguide arrays (MW1 and MW2), the CO_2 laser scattering diagnostics, and two sets of double full-poloidal ring limiters.

The plasma density at the limiter radius, which was at most 1/3 of the peak density, has been measured with Langmuir probes in carbon limited discharges. For a line-average density of $\overline{n}_e = 2 \times 10^{14}\,\mathrm{cm}^{-3}$, the plasma density at the main limiter radius $a = 16.5\,\mathrm{cm}$, was $n_e \lesssim 1 \times 10^{14}\,\mathrm{cm}^{-3}$ and fell exponentially to $5 \times 10^{12}\,\mathrm{cm}^{-3}$ at the secondary limiter (radius of $r = 18\,\mathrm{cm}$) where the face of the waveguide array is normally located. The edge density is not a simple function of the line-average density and is also dependent on the port location. The electron temperature varies from $T_e \gtrsim 20\,\mathrm{eV}$ at the main limiter radius to $T_e \lesssim 5\,\mathrm{eV}$ at the secondary limiter radius. These measured profiles were used to calculate the growth rates in Fig. 5.

A. Low-Frequency Fluctuations and Pump Broadening

A large level of low-frequency density fluctuations was observed in the shadow of the main limiter when the probe was biased to collect ion-saturation current. Typically, $\delta n/n \simeq O(1/2)$ where δn is the amplitude of the fluctuating component

of the density and n is the time-averaged density. The spectral shape was roughly exponential with the $1/e$ width in the range 150–200 kHz, with little dependence on density, magnetic field, or ion species. Similar density fluctuations were observed with CO_2 laser scattering near the main limiter radius. The frequency width obtained with scattering was an increasing function of k.[15]

The frequency spectra above 1 MHz were studied with floating rf probes located at $r = 17.8$ cm. The frequency spectra depended on the location of the probe with respect to the wave launcher. In Fig. 8 we show the pump frequency spectra ($f \simeq f_0 \pm 20$ MHz), obtained at three different toroidal locations when the wave was launched by a four-waveguide array located at the C-port (see Fig. 7 for port locations). Spectrum (a) was obtained with the probe located right in front of the waveguide array, whereas spectra (b) and (c) were obtained at the D- and F-ports (60° and 180° away toroidally from the waveguide array). Surface waves which cannot propagate beyond the main limiter radius into the plasma interior cannot reach the location (c) because these waves will be reflected from the full-poloidal main limiters located at both B- and E-ports. We interpret the sharp peak at the pump frequency to be due to these surface waves. The broadband background feature is fairly independent of probe position and we interpret it to be due to waves that have propagated out to the location of the probe from the plasma interior. These waves had to have undergone intense scattering from the turbulent low-frequency density fluctuations. In the remainder of this paper, we shall present only the data obtained with rf probes located 180° away toroidally from the wave launcher, which we believe give the best indication of wave spectra characteristic of the plasma interior.

We show the frequency width (FWHM) of the broadened pump wave as a function of density for deuterium and hydrogen plasmas in Figs. 9(a) and (b). The

frequency width is independent of the magnetic field, and is also fairly independent of the injected rf power level. There is also a frequency down-shift of the order of 1 MHz except at low densities, $\overline{n}_e \lesssim 1 \times 10^{14}\,\mathrm{cm}^{-3}$, where the spectrum is symmetric about the pump frequency. In Figs. 10(a) and (b) we show the spectra of the low-frequency potential fluctuations before and during the rf pulse. There is significant increase in the fluctuation level in the range of a few MHz. There is a threshold density $\overline{n}_e \simeq 1 \times 10^{14}\,\mathrm{cm}^{-3}$ below which this enhancement in the potential fluctuations is absent. There is also a power threshold of a few tens of kW for this enhancement. These results suggest that parametric decay into ion-sound quasimodes[10] may be occurring. We note that neither the ion density fluctuation observed on ion saturation current nor the electron density fluctuation observed by CO_2 laser scattering change appreciably in the same frequency range with the application of rf power.[18] These results are not in contradiction with parametric excitation of ion-sound quasimodes,[18] but exclude the possibility that this potential fluctuation enhancement is entirely due to enhancement in drift wave turbulence. The frequency broadening of the pump is due to scattering from low-frequency density fluctuations[14] at densities below threshold. It is not clear at present how much broadening, if any, is due to parametric decay at densities above threshold.

B. Ion-Cyclotron Sidebands

The high-frequency and low-frequency spectra over a wider frequency range at two different densities, one above and one below threshold, are shown in Figs. 11(a) and (b). The ion-cyclotron peaks are separated from each other by less than the central ion-cyclotron frequency, but slightly greater than the ion-cyclotron frequency evaluated at the outside (larger major radius side) edge of the torus, suggesting that these sidebands were generated near the outside plasma edge, not too far from the

waveguide array. The spacing between ion-cyclotron peaks is independent of the probe location along the major radius in the range $52 \leq R \leq 76\,\mathrm{cm}$ (the major radius of the torus R_0 is 64 cm). There are two distinct features in the high-frequency spectrum of Fig. 11(a). Based on our numerical results presented in the last section, we interpret the first few harmonic lower-sidebands to be due to parametric decay into ion-cyclotron quasimodes ($\omega \simeq n\omega_{ci}$) near the plasma edge where the temperature is low, and the higher harmonics, peaked around $|\omega^-|/\omega_0 \simeq 0.85$, to be due to parametric decay into nonresonant quasimodes $[\omega/k_\parallel v_{te} \simeq O(1)]$ excited farther inside where the temperature is higher.[19] The higher harmonics have a higher density threshold than the lower harmonics. In contrast to the lower-sideband spectrum, the low-frequency spectrum is always monotonically decreasing and never shows a peak at $\omega/\omega_0 \simeq 0.15$. In Alcator C, the dominant peak is almost always the first ion-cyclotron lower-sideband. Under the condition of Fig. 11(b), which we claim to be below the threshold density, there exists an unstable mode at $\omega = \omega_{ci}$ (again, evaluated at the outside edge) in the Ohmic plasma. The origin of this mode is not clear at present. The pump wave is significantly narrower, and more or less symmetric lower- and upper-sidebands are observed. We believe that rather than being due to parametric decay, these sidebands are produced by the passive nonlinear beating of the lower hybrid wave on a pre-existing marginally unstable ion-cyclotron wave. The amplitudes of these modes are small (50 dB down from the pump) in contrast to the parametric modes in Fig. 11(a). If these ion-cyclotron modes were only marginally stable in the density regime where we observe parametric decay, there is a possibility that they might be driven unstable in the presence of the pump wave, thus reducing the threshold for parametric decay.

In Fig. 12 we show the frequency-integrated pump power (including the broadening of a few MHz) and sideband power (integrated over all sidebands) as functions

of density. Above the threshold density of $\overline{n}_e \simeq 1.5 \times 10^{14}\,\mathrm{cm}^{-3}$, the sideband power reaches about 30% of the pump power. and both sideband and pump powers decrease rapidly with density. In Fig. 13 we show the pump and sideband powers as functions of injected rf power. Above the threshold rf power of 10 kW the sideband rises to about 30% of the pump power, and both sideband and pump powers keep increasing linearly with rf power. Therefore, we cannot conclude that pump depletion due to parametric decay has occurred. The decrease of the pump wave power at high densities may partially be due to increased collisional damping near the plasma edge.[20]

C. Ion Tail Formation

The correlation between ion tail formation and parametric decay was studied with a mass-resolving charge exchange neutral analyzer located at the E-port (see Fig. 7).[3,4] The charge exchange (CX) analyzer viewed the plasma perpendicularly from the larger major radius side through the gap between a pair of main limiters located at this port. The CO_2 laser scattering diagnostics was also located at this port. The two waveguide arrays were located 60° (MW2) and 120° (MW1) away toroidally from this port. The ion tails were observed only above the sharp density threshold of $\overline{n}_e \simeq 1.5 \times 10^{14}\,\mathrm{cm}^{-3}$ in hydrogen [corresponding to $\omega_0/\omega_{LH}(0) = 1.8$ and $\omega_0/\omega_{LH}(a) = 2.9$], and $\overline{n}_e \simeq 2.0 \times 10^{14}\,\mathrm{cm}^{-3}$ in deuterium [$\omega_0/\omega_{LH}(0) = 2.2$ and $\omega_0/\omega_{LH}(a) = 3.6$], both at $B = 9\,\mathrm{T}$. This is shown in Figs. 14(a) and (b) where the ion tail "temperature" is plotted as a function of density. Here, typical experimental values of $n_e(0)/\overline{n}_e = 1.3$ and $n_e(a)/n_e(0) = 0.3$ have been used to evaluate ω_{LH}. In general, stronger ion tails were observed in hydrogen plasmas than in deuterium plasmas. In general, stronger ion tails were observed when the lower-hybrid waves were injected from MW2 (the closer of the two arrays) rather

than MW1, as shown with the open symbols in Fig. 14(b). The fast decay time of the high energy CX neutral flux and the absence of neutron rate enhancement in the case of deuterium plasmas imply that the ion tails did not originate from the plasma center. These density thresholds for ion tail formation correlated well with the onset of strong parametric decay observed by rf probes. The frequency-integrated sideband powers observed by the rf probe during the same runs are shown in Figs. 15(a) and (b). These results suggest that ion tails are created near the plasma edge through the excitation of parametric decay, and that this effect is localized toroidally near the wave launching location. This toroidal localization is supported by the CO_2 laser scattering data which will be presented in the next section.

IV. CO_2 LASER SCATTERING MEASUREMENTS

A. Experimental Setup

Here we present results from CO_2 laser scattering from the first-harmonic ion-cyclotron lower-sideband.[3] As mentioned earlier, according to rf probe measurements, this is almost always the dominant peak in the Alcator C experiments. Higher harmonic sidebands were not studied with scattering. The scattering volume was located at the E-port (see Fig. 7), 120° from MW1 and 60° from MW2 toroidally. A relative waveguide phasing of 180° was used in the present experiments. The experimental configuration is shown schematically in Fig. 16. The local oscillator (LO) beam which is needed for heterodyne detection,[21] passed vertically through the plasma at a distance $x \equiv R - R_0$ from the plasma center along the major radius, and was held fixed during a k scan to ensure constant detection efficiency. The main laser beam was oriented parallel to the LO beam at mirror M1 and the two beams were made to cross at the focus of lens L2, which was located inside the plasma volume. The main laser beam, scattered in the direction of the LO beam, was detected and optically mixed with the LO beam at the detector (Ge:Cu photomixer). By translating the mirror M1 vertically, the separation between the two beams could be altered. The spacing between the two beams d, and the focal length f of the lens L2 determines the scattering angle $\phi_s \simeq d/f$, and therefore the wave number of the wave being studied $k \simeq k_i \phi_s$, where k_i is the wave number of the CO_2 laser beam. We note that in the present configuration only waves with wave vector $\mathbf{k}$ oriented along the major radius could be detected. The typical range of wave numbers studied were in the range $80 \leq k \leq 240\,\mathrm{cm}^{-1}$. The waist radius of the laser beam at the focus was 0.1 cm, which gives a horizontal spatial resolution of ± 0.1 cm and a wave number resolution of $\pm 20\,\mathrm{cm}^{-1}$. The vertical spatial

resolution varies inversely with k and was measured to be $\pm 10\,\mathrm{cm}$ at $k = 80\,\mathrm{cm}^{-1}$ (at $k = 200\,\mathrm{cm}^{-1}$ it would be $\pm 4\,\mathrm{cm}$).[17] The scattered signal was analyzed using a 16-channel filter bank for the pump wave and an 8-channel filter bank for the first ion-cyclotron harmonic lower-sideband wave (or simply referred to here as the decay wave).

B. Scattering Results

Typical frequency spectra of the pump wave (ω_0) and the decay wave (first ion-cyclotron lower-sideband, $\omega_0 - \omega_{ci}$) are shown in Figs. 17(a) and (b). The decay wave has a wider frequency width than the pump wave by a factor of 2 to 3. In general, the pump wave frequency spectrum observed by CO_2 laser scattering in the plasma interior is very similar to that observed by an rf probe located at the plasma edge provided that the probe is insensitive to the surface waves. As an example, we compare in Fig. 18 the density dependence of the frequency width (HWHM) of the broadened pump wave obtained by an rf probe located 180° away toroidally from the wave launcher, with that obtained by CO_2 laser scattering at $x = +5\,\mathrm{cm}$ and at $k = 80\,\mathrm{cm}^{-1}$.[22] (The frequency width obtained with scattering is an increasing function of k.[17]) This observation supports our interpretation that these probes are sensitive to waves that have escaped out from the plasma interior. The frequency difference between the pump wave and the decay wave is again less than the central ion-cyclotron frequency but slightly greater than the ion-cyclotron frequency at the outside edge. As shown in Fig. 19 the decay wave has been observed only within a narrow density band. The pump wave also becomes unobservable slightly above the upper end of this density band. This density band does not exactly coincide with the density range where the rf probes detect the decay waves. There is some evidence that this density band moves slightly towards lower density at

a lower plasma current, but this dependence has not been studied in detail. The dependences of the scattered powers from the pump and decay waves on injected rf power are shown in Fig. 20. In this particular case the decay wave is observed above a threshold rf power of $P_{\rm rf} \simeq 100\,{\rm kW}$, which is an order of magnitude lower than the convective threshold estimated in Sec. II–B. There is no evidence of pump depletion due to parametric decay by the time the pump wave reaches $x/a = +3/4$ and 60° away toroidally from the wave launcher.

In the present experiments the scattering volumes were located along the vertical chords at major radial locations $x \equiv R - R_0 = 0,\ +5,\ +12\,{\rm cm}$ (the limiter radius is $a = 16.5\,{\rm cm}$). In addition, a vertical scan was also carried out at $x = 0\,{\rm cm}$. In general, the largest scattered decay wave signal is observed at the location where the largest scattered pump wave signal is observed. The largest scattered signals (for both the pump wave and the decay wave) were observed at $x = +12\,{\rm cm}$. This is the location that the pump wave is expected to be observed (*i.e.*, the toroidal and poloidal locations as well as the wave number orientation are correct) according to the predictions of the toroidal ray tracing code with scattering from density fluctuations included.[17] The decay wave is also expected to be observed where the pump wave is observed since the maximum growth rate is obtained for those decay waves that have traveled inside the pump "resonance cone". However, no significant decay wave signals were observed at vertical positions $y = \pm 12\,{\rm cm}$ at $x = 0\,{\rm cm}$, which correspond to the same minor radial positions ($r = 12\,{\rm cm}$) as $x = +12\,{\rm cm}$ and $y = 0\,{\rm cm}$ where the largest decay wave signals were observed. The intensity of the scattered signal from the pump wave was also significantly lower at $(x, y) = (0, \pm 12)$ than at $(x, y) = (+12, 0)$. One has to be careful in comparing the relative decay wave (or pump wave) powers at these different locations since scattering samples different regions of real space and $\mathbf{k}$ space. At $(x, y) = (+12, 0)$ scattering is sensitive

to waves with $k_r \gg k_\theta$, whereas at $(x, y) = (0, \pm 12)$ it is sensitive to waves with $k_\theta \gg k_r$, where k_r and k_θ are the radial and poloidal components of the wave vector $\mathbf{k}$. Only the waves with correct wave vector orientation are observable with scattering. In addition, at both locations the scattering volume is much larger in the vertical direction than in the horizontal direction. The two waveguide arrays located at different toroidal positions (MW1 and MW2, see Fig. 7) permit us to study the toroidal localization of the decay process. (Again, we have to be aware of the fact that the wave vector orientation must be nearly perpendicular to the laser beam in order for the wave to be observable by scattering.) No significant levels of decay waves have been observed by laser scattering at any radial location studied when the lower-hybrid waves were injected from MW1 alone. We note that the scattered pump wave signal was also typically an order of magnitude higher from MW2 than from MW1 at $x = +12\,\mathrm{cm}$.[17] In addition, as discussed in the last section, much stronger ion tails (observed at the same port as the CO_2 laser scattering) were observed when the waves were injected from MW2, which confirms our belief that the ion tails were created through the excitation of parametric decay. In summary, from the scattering data it appears that the decay waves are localized in the poloidal cross section near the outside plasma edge $x \gtrsim +12\,\mathrm{cm}$, and also localized toroidally to $\lesssim 90°$ from the waveguide array.

The power density spectrum, $P(N_{||})$, was deduced from the scattered power spectrum $P_{\mathrm{sc}}(k)$ by using the warm-plasma dispersion relation, including electromagnetic effects, to relate k to $N_{||}$ (where $N_{||} \equiv ck_{||}/\omega$ is the index of refraction parallel to the magnetic field). The scattered power (which is proportional to $\tilde{n}_e^2$) was rescaled in terms of the wave power density.[23] In order to obtain $N_{||}$ from k, a knowledge of the local density is necessary. Since scattering measures volume integrated scattered power inside the scattering volume whose vertical dimension

could be large (especially for small scattering angles), a unique mapping of k into $N_{\|}$ cannot be made. Rather, a single value of k corresponds to a range of $N_{\|}$'s. Therefore, we shall denote by $N_{\|}^{\sim}$ the value of $N_{\|}$ obtained by using the density at the midplane of the torus. The data presented in this paper will be in terms of $N_{\|}^{\sim}$. A value of $N_{\|}^{\sim}$ gives a lower bound on the true value of $N_{\|}$. Some discussion on differences between the average value of $N_{\|}$ (based on numerical simulations) and $N_{\|}^{\sim}$ is given in Ref. 17. In the present case this difference $(N_{\|} - N_{\|}^{\sim})/N_{\|}$ should be smaller than for the case of Ref. 17 since due to the larger values of k, the vertical resolution is better.

The power density spectra $P(N_{\|}^{\sim})$ for the pump wave and for the decay wave deduced from the experimentally measured k-spectra are shown in Fig. 21. These data were obtained at $x = +12\,\mathrm{cm}$ $(x/a \simeq +3/4)$, and from three separate k-scans covering the range $80 \lesssim k \lesssim 240\,\mathrm{cm}^{-1}$. Data from the different k-scans have been scaled in amplitude to compensate for the different optical alignments used in each scan. It can be seen that the decay wave power is concentrated at higher values of $N_{\|}^{\sim}$ $(N_{\|}^{\sim} \simeq 7)$ than the pump wave. The measured k-spectrum of the decay wave is consistent with parametric excitation of ion-cyclotron quasimodes. The pump wave spectrum at this location and this waveguide phasing is peaked at $N_{\|}^{\sim} \simeq 2.6$ (which corresponds to the average value of $N_{\|} \simeq 3$ based on numerical modeling).[17] As noted earlier, the difference between $N_{\|}^{\sim}$ and the average value of $N_{\|}$ (which is due to uncertainty in the local plasma density) is less for the present case since the vertical resolution is better at larger values of k. If we assume that the $\mathbf{k}_{\perp}$ distributions of both the pump wave and the decay wave are isotropic in the perpendicular plane the frequency- and wave number-integrated power in the decay wave is at most 3% that of the pump wave. This would be an under-estimate of the relative decay wave power compared to the pump wave power if $k_r \gg k_\theta$ for the pump wave and/or

$k_\theta \gg k_r$ for the decay wave. Similarly, there could be significantly more power contained in higher ion-cyclotron harmonic sidebands which were not studied by scattering in the present experiments.

The wave number of the decay wave is characterized by $|k^-| \lesssim 190\,\mathrm{cm}^{-1}$ which is consistent with the condition $|\omega^-/k_\parallel^- v_{te}| \gtrsim 4$ at $x/a \simeq +3/4$ where $T_e \simeq 250\,\mathrm{eV}$. The decay wave observed at $x/a = +3/4$ probably originated near the waveguide mouth and propagated inside the pump "resonance cone". Therefore, growth of the decay wave is influenced by the growth rates at all locations between the waveguide mouth and the observation point. In general, the local growth rate is an increasing function of $|n_\parallel^-|$ up to the Landau damping limit $|n_\parallel^-| \lesssim c/4v_{te}$. While the decay waves with larger values of $|n_\parallel^-|$ may have larger growth rates at larger minor radii where the electron temperature is lower, they are heavily Landau damped by the time they reach the observation point. Consequently, the wave number spectrum is determined by the electron temperature at the observation point. The observed wave number of the lower-sideband decay wave (as well as the pump wave number) is too small to create ion tails at this location since $|\omega^-/k_\perp^- v_{ti}| \gtrsim 10$ if we take $T_i \simeq 250\,\mathrm{eV}$ at $r = 12\,\mathrm{cm}$. However, according to our theoretical predictions the low-frequency ion-cyclotron quasimodes are always strongly damped by ions. Therefore, the ion tails observed by charge exchange are most likely created by ion-cyclotron damping of the quasimodes.

V. SUMMARY AND CONCLUSIONS

Using rf probes and CO_2 laser scattering we have observed parametric decay instabilities at relatively high densities $\omega_0/\omega_{LH}(0) \lesssim 2$ in the Alcator C tokamak. The pump wave data obtained with rf probes sufficiently far from the rf source are consistent with CO_2 laser scattering data obtained in the plasma interior. However, there are some differences in the decay wave data obtained with the two techniques. Comparison of the probe frequency spectra with our numerical analysis suggest that parametric excitations of ion-cyclotron quasimodes, nonresonant quasimodes, and possibly ion-sound quasimodes are taking place. The onset of strong parametric decay is well correlated with ion tail formation near the plasma edge. The decay region is located near the outside (larger major radius side) edge, $x/a \gtrsim +3/4$, and localized toroidally near the wave launcher. The decay wave has been observed by CO_2 laser scattering only where strong pump wave signals are also observed. The ion tails are believed to be caused by heavily ion-cyclotron damped quasimodes. The measured wave number spectrum of the lower-sideband wave at $x/a = +3/4$ is peaked at higher values of k (and hence $N_{||}$) than the pump wave spectrum, the peak being determined by electron Landau damping at the lower-sideband at the observation point. The experimentally observed threshold rf power for parametric decay is an order of magnitude lower than the theoretically predicted convective threshold. The reason for this discrepancy is not clear at present. A significant fraction ($\simeq$ 30%) of the wave power may be deposited near the plasma surface through excitation of parametric decay at high densities when $\omega_0/\omega_{LH}(0) \lesssim 2$. A conclusive verification of pump wave depletion due to parametric decay instabilities was not demonstrated here. It is possible that some other mechanism(s) may be playing a key role in preventing pump wave penetration, and central ion heating, when the density is sufficiently high for the lower-hybrid mode conversion layer to

be present near the plasma center. However, before more definite conclusions on the role of parametric decay upon pump wave penetration can be drawn, further laser scattering measurements of the higher ion-cyclotron harmonic sidebands will have to be carried out.

ACKNOWLEDGMENTS

We thank the Alcator operating crew and the experimental team for their support in carrying out these experiments. The CO_2 laser scattering experiment was originally set up by Drs. R. E. Slusher and C. M. Surko. One of the filter banks used for the scattering experiment was on loan from Princeton Plasma Physics Laboratory. This work was supported by the U.S. Department of Energy. Contract No. DE-AC02-78ET51013.

FOOTNOTES AND REFERENCES

[a)]Now at Raytheon Company, Wayland, Massachusetts 01778.

[1]W. Hooke, Plasma Physics and Controlled Fusion **26**, 133 (1984) and references therein.

[2]M. Porkolab, J. J. Schuss, Y. Takase, S. Texter, B. Blackwell, C. Fiore, R. Gandy, R. S. Granetz, M. Greenwald, D. Gwinn, B. Lipschultz, E. S. Marmar, S. McCool, D.S. Pappas, R. R. Parker, P.Pribyl, J. E. Rice, J. L. Terry, R. Watterson, and S. M. Wolfe, in *Plasma Phys. and Controlled Nucl. Fusion Research* 1982 (9th Conf. Proc., Baltimore, 1982) (IAEA, Vienna, 1983), Vol. I, p. 227; M. Porkolab, B. Lloyd, J. J. Schuss, Y. Takase, S. Texter, R. Watterson, P. Bonoli, R. Englade, C. Fiore, R.. Gandy, R. Granetz, M. Greenwald, D. Gwinn, B. Lipschultz, E. Marmar, S. McCool, D. Pappas, R. Parker, P. Pribyl, J. Rice, J. Terry, and S. Wolfe, in *Controlled Fusion and Plasma Phys.* (Proc. 11th Eur. Conf., Aachen, W. Germany, 1983) (Eur. Phys. Soc., Petit-Lancy, Switzerland, 1983), Vol. 7-D, Part I, p. 269.

[3]Y. Takase, R. L. Watterson, M. Porkolab, C. L. Fiore, R. E. Slusher, and C. M. Surko, Phys. Rev. Lett. **53**, 274 (1984).

[4]C. L. Fiore, M. J. Greenwald, S. V. Judd, Y. Takase, B. Lloyd, M. Porkolab, and J. Schuss, Bull. Am. Phys. Soc. **28**, 1163 (1983).

[5]M. Porkolab, Phys. Fluids **17**, 1432 (1974).

[6]M. Porkolab, Phys. Fluids **20**, 2058 (1977).

[7]R. L. Berger, L. Chen, P. K. Kaw, and F. W. Perkins, Phys. Fluids **20**, 1864 (1977).

[8]E. Villalon and A.Bers, Nucl. Fusion **20**, 243 (1980).

[9]C. S. Liu, V. S. Chan, V. K. Tripathi, and V. Stefan, G. A. Technologies Report GA-A17019 (1983).

[10]Y. Takase and M. Porkolab, Phys. Fluids **26**, 2992 (1983).

[11]S. Fairfax, A. Gondhalekar, R. Granetz, M. Greenwald, D. Gwinn, I. H. Hutchinson, S. E. Kissel, B. Lipschultz, E. S. Marmar, D. O. Overskei, D. S. Pappas, J. Parker, R. R. Parker, P. A. Pribyl, J. E. Rice, J. J. Schuss, N. Sharky, R. J. Temkin, J. L. Terry, R. Watterson, S. M. Wolfe, S. L. Allen, J. Castracane, and W. Hodge, in *Plasma Phys. and Controlled Nucl. Fusion Research* 1980 (8th Conf. Proc., Brussels, 1980) (IAEA, Vienna, 1981), Vol. I, p. 439.

[12]E. Ott, Phys. Fluids **22**, 1732 (1979).

[13]P. T. Bonoli and E. Ott, Phys. Fluids **25**. 359 (1982).

[14]P. L. Andrews and F. W. Perkins, Phys. Fluids **26**, 2537 and 2546 (1983).

[15]R. L. Watterson, T. R. Gentile, R. E. Slusher, and C. M. Surko, Bull. Am. Phys. Soc. **27**, 937 (1981).

[16]M. N. Rosenbluth, Phys. Rev. Lett. **29**, 565 (1972).

[17]R. L. Watterson, Y. Takase, P. T. Bonoli, M. Porkolab, R. E. Slusher, and C. M. Surko, MIT Plasma Fusion Center Report PFC/JA-84-6; submitted to Physical Review Letters.

[18]Y. Takase, Sc. D. Thesis, Massachusetts Institute of Technology (1983); MIT Plasma Fusion Center Report PFC/RR-83-29 (unpublished).

[19]M. Porkolab, S. Bernabei, W. M. Hooke, R. W. Motley, and T. Nagashima, Phys. Rev. Lett. **38**, 230 (1977).

[20]P. T. Bonoli, IEEE Transactions on Plasma Science, Vol. PS-12, p. 95 (1984).

[21]R. E. Slusher and C. M. Surko, Phys. Fluids **23**, 472 (1980).

[22]R. L. Watterson, Y. Takase, B. Lloyd, M. Porkolab, J. J. Schuss, R. E. Slusher, and C. M. Surko, Bull. Am. Phys. Soc. **28**, 1162 (1983).

[23]R. E. Slusher, C. M. Surko, J. J. Schuss, R. R. Parker, I. H. Hutchinson, D.

Overskei, and L. S. Scaturro, Phys. Fluids **25**, 457 (1982).

FIGURE CAPTIONS

Fig. 1. Numerical solution of the parametric dispersion relation for a deuterium plasma, $B = 6.7\,\mathrm{T}$, $n_e = 1.9 \times 10^{14}\,\mathrm{cm}^{-3}$, $T_e = T_i = 250\,\mathrm{eV}$, $P_{\mathrm{rf}} = 100\,\mathrm{kW}$, $ck_{0\|}/\omega_0 = 3$, and $ck_{\|}^{-}/\omega_0 = 7$, which were typical parameters near $r/a \simeq 3/4$ when CO_2 scattering data were obtained. (a) γ and ω_R of the quasimode ($\omega \equiv \omega_R + i\gamma$) as functions of k of the quasimode, (b) γ as a function of ω_R.

Fig. 2. The dependence of $\omega_{R\max}$ and $\gamma_{\max}$ on density. Hydrogen plasma, $B = 10\,\mathrm{T}$, $T_e = T_i = 20\,\mathrm{eV}$, $P_{\mathrm{rf}} = 100\,\mathrm{kW}$, $ck_{0\|}/\omega_0 = 3$, and $ck_{\|}^{-}/\omega_0 = 5$.

Fig. 3. The dependence of $\omega_{R\max}$ and $\gamma_{\max}$ on T_e. The straight line corresponds to $\omega_{R\max} \simeq 0.4k_{\|}v_{te}$. Hydrogen plasma, $B = 10\,\mathrm{T}$, $n_e = 1 \times 10^{14}\,\mathrm{cm}^{-3}$ ($\omega_0/\omega_{LH}(0) = 2.3$), $P_{\mathrm{rf}} = 100\,\mathrm{kW}$, $ck_{0\|}/\omega_0 = 3$, and $ck_{\|}^{-}/\omega_0 = 5$.

Fig. 4. The dependence of $\omega_{R\max}$ and $\gamma_{\max}$ on $k_{\|}$. The straight line corresponds to $\omega_{R\max} \simeq 0.4k_{\|}v_{te}$. Hydrogen plasma, $B = 10\,\mathrm{T}$, $n_e = 1 \times 10^{14}\,\mathrm{cm}^{-3}$ ($\omega_0/\omega_{LH}(0) = 2.3$), $T_e = T_i = 50\,\mathrm{eV}$, $P_{\mathrm{rf}} = 400\,\mathrm{kW}$, and $ck_{0\|}/\omega_0 = 3$.

Fig. 5. The dependences of $\gamma_{\max}$ and $\omega_{R\max}$ as functions of the major radial distance from the plasma center $x \equiv R - R_0$ for typical Alcator C parameters when CO_2 scattering data were obtained, namely, deuterium plasma, $B = 8\,\mathrm{T}$, $\bar{n}_e = 2.1 \times 10^{14}\,\mathrm{cm}^{-3}$, $T_{e0} = 1.5\,\mathrm{keV}$, $P_{\mathrm{rf}} = 100\,\mathrm{kW}$, $ck_{0\|}/\omega_0 = 3$, and $ck_{\|}^{-}/\omega_0 = 7$. The triangles show the growth rate for $\theta = \pi/2$ (mainly $\mathbf{E} \times \mathbf{B}$ coupling) whereas the crosses show the growth rate for $\theta = 0$ ($E_{\|}$ coupling).

Fig. 6. The dependence of the growth rate of the first ion-cyclotron quasimode ($\omega_R \simeq \omega_{ci}$) on rf power. The straight lines plotted correspond to $\gamma \propto P_{\mathrm{rf}}^{0.75}$ and $\gamma \propto P_{\mathrm{rf}}^{0.6}$. Hydrogen plasma, $B = 10\,\mathrm{T}$, $n_e = 1 \times 10^{14}\,\mathrm{cm}^{-3}$ ($\omega_0/\omega_{LH}(0) = 2.3$), $T_e = T_i = 50\,\mathrm{eV}$, $ck_{0\|}/\omega_0 = 3$, and $ck_{\|}^{-}/\omega_0 = 5$.

Fig. 7. Locations of the waveguide arrays, limiters, and relevant diagnostics.

Fig. 8. The frequency spectra near the pump frequency $f_0 = 4.6\,\mathrm{GHz}$ obtained

with rf probes at three different toroidal locations: (a) C-port (in front of the waveguide array), (b) D-port (60° away), and (c) F-port (180° away). Deuterium, $B = 8\,\mathrm{T}$, $\bar{n}_e = 3.4 \times 10^{14}\,\mathrm{cm}^{-3}$ ($\omega_0/\omega_{LH}(0) = 1.9$), and $P_{\mathrm{rf}} = 40\,\mathrm{kW}$.

Fig. 9. The frequency width (FWHM) of the broadened pump wave as a function of density for (a) deuterium and (b) hydrogen plasmas.

Fig. 10. The spectra of the low-frequency potential fluctuations (a) before and (b) during the rf pulse. Deuterium, $B = 8\,\mathrm{T}$, $\bar{n}_e = 1.4 \times 10^{14}\,\mathrm{cm}^{-3}$ ($\omega_0/\omega_{LH}(0) = 2.6$), and $P_{\mathrm{rf}} = 140\,\mathrm{kW}$.

Fig. 11. The low-frequency (left) and high-frequency (right) spectra at two different densities. Hydrogen, $B = 8\,\mathrm{T}$, (a) $\bar{n}_e = 2.1 \times 10^{14}\,\mathrm{cm}^{-3}$ ($\omega_0/\omega_{LH}(0) = 1.6$), and (b) $\bar{n}_e = 1.1 \times 10^{14}\,\mathrm{cm}^{-3}$ ($\omega_0/\omega_{LH}(0) = 2.0$).

Fig. 12. The frequency-integrated pump power (including the pump broadening) and sideband power (integrated over all sidebands) as functions of density. Deuterium, $B = 8\,\mathrm{T}$, and $P_{\mathrm{rf}} = 280\,\mathrm{kW}$.

Fig. 13. The frequency-integrated pump and sideband powers as functions of injected rf power. Hydrogen, $B = 8\,\mathrm{T}$, and $\bar{n}_e = 2.6 \times 10^{14}\,\mathrm{cm}^{-3}$ ($\omega_0/\omega_{LH}(0) = 1.5$).

Fig. 14. The ion tail "temperature" as a function of density in (a) hydrogen and (b) deuterium plasmas.

Fig. 15. The frequency-integrated sideband power as a function of density in (a) hydrogen and (b) deuterium plasmas (different absolute scales) obtained during the same runs as Fig. 14.

Fig. 16. The CO_2 scattering configuration.

Fig. 17. Typical frequency spectra of (a) the pump wave (ω_0) and (b) the decay wave ($\omega_0 - \omega_{ci}$). Deuterium, $B = 8\,\mathrm{T}$, $\bar{n}_e = 3.7 \times 10^{14}\,\mathrm{cm}^{-3}$, $P_{\mathrm{rf}} = 280\,\mathrm{kW}$, $x = +12\,\mathrm{cm}$, and $k = 150\,\mathrm{cm}^{-1}$.

Fig. 18. The density dependence of the frequency width (HWHM) of the pump

wave observed by scattering (at $x = +5\,\mathrm{cm}$, $k = 80\,\mathrm{cm}^{-1}$) and rf probe. The probe was located 180° away toroidally from the wave launcher so that it is insensitive to the surface waves. Deuterium, $8 \leq B \leq 10\,\mathrm{T}$.

Fig. 19. The density band over which the decay wave has been observed by CO_2 scattering. Deuterium, $B = 8\,\mathrm{T}$, $P_{\mathrm{rf}} = 300\,\mathrm{kW}$, $x = +14\,\mathrm{cm}$, and $k = 140\,\mathrm{cm}^{-1}$.

Fig. 20. The dependences of the scattered powers from the pump and decay waves on injected rf power. Deuterium, $B = 8\,\mathrm{T}$, $\bar{n}_e = 2.1 \times 10^{14}\,\mathrm{cm}^{-3}$, $x = +12\,\mathrm{cm}$, and $k = 150\,\mathrm{cm}^{-1}$. The pump wave data points are scaled down by a factor of 10.

Fig. 21. The power density spectra $P(N_{\|}^{*})$ for the pump wave and for the decay wave deduced from the experimentally measured k-spectra. Deuterium, $B = 8\,\mathrm{T}$, $1.8 \leq \bar{n}_e(10^{14}\,\mathrm{cm}^{-3}) \leq 2.4$, $P_{\mathrm{rf}} = 260\,\mathrm{kW}$, and $x = +12\,\mathrm{cm}$. The pump wave data points are scaled down by a factor of 20. $N_{\|}^{*}$ is defined in the text.

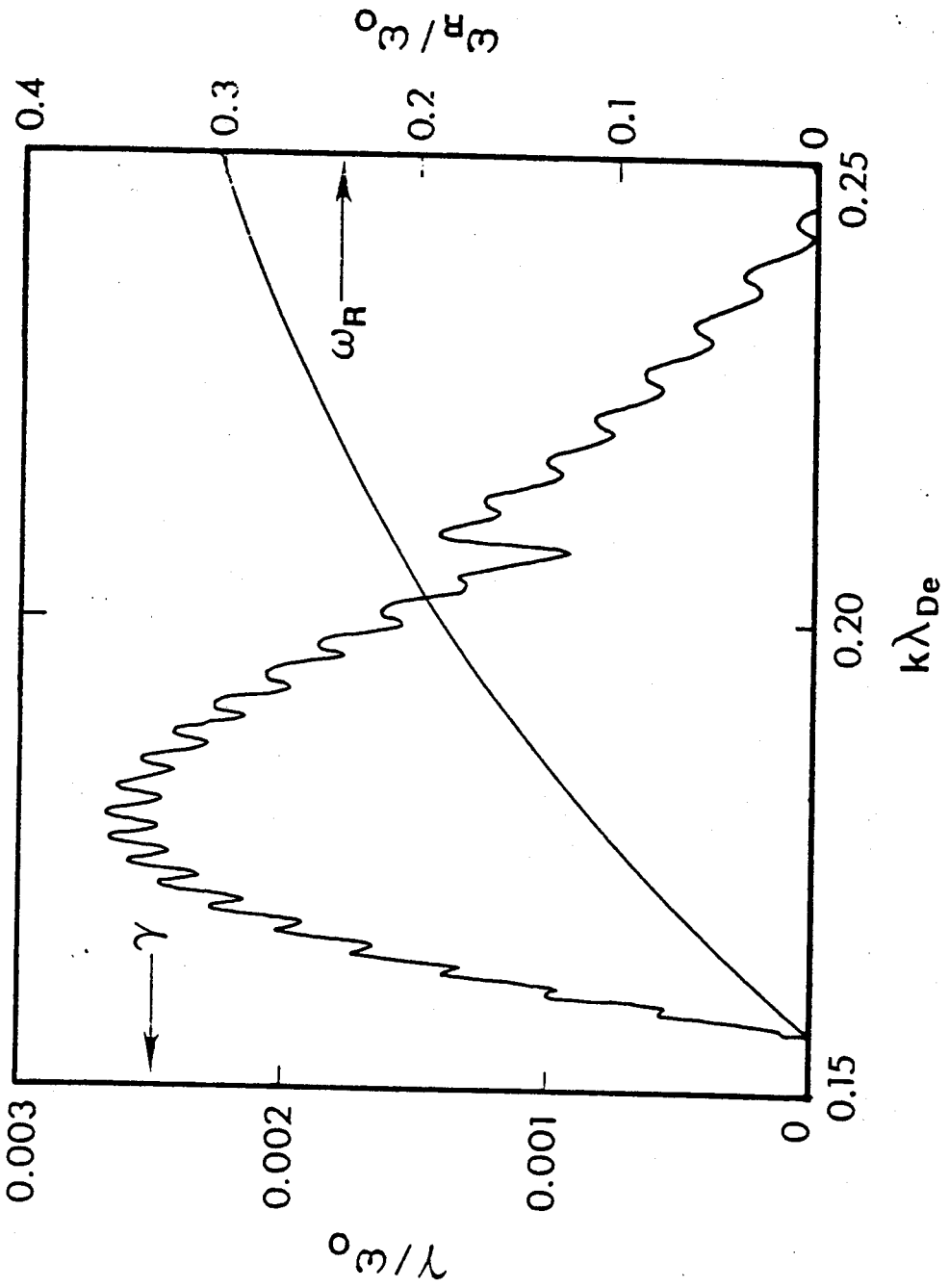
ω_R/ω_0
0.4
0.3
0.2
0.1
0
ω_R
0.25
0.20
0.15
$k\lambda_{De}$
γ
0.003
0.002
0.001
0
γ/ω_0

Fig. 1(a)

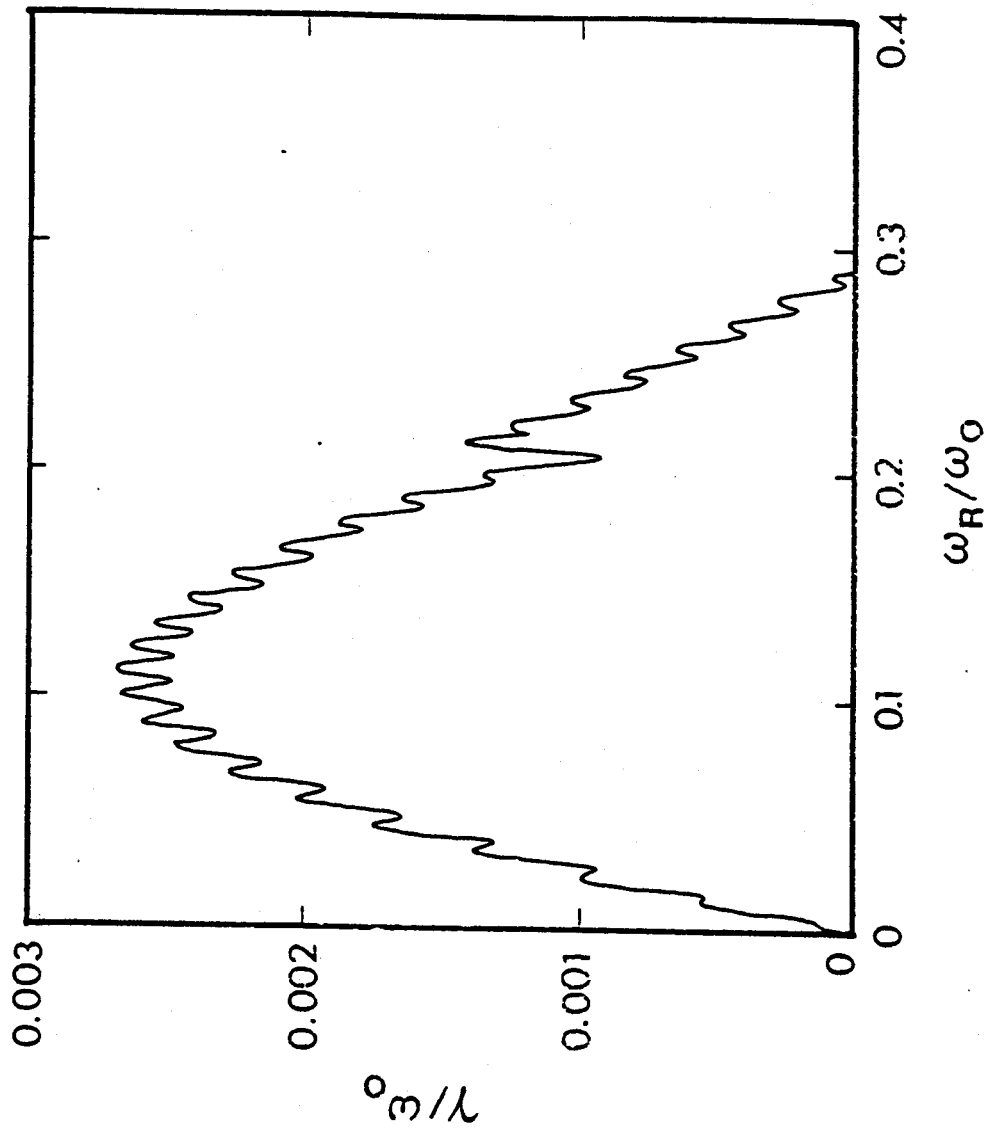

Fig. 1(b)

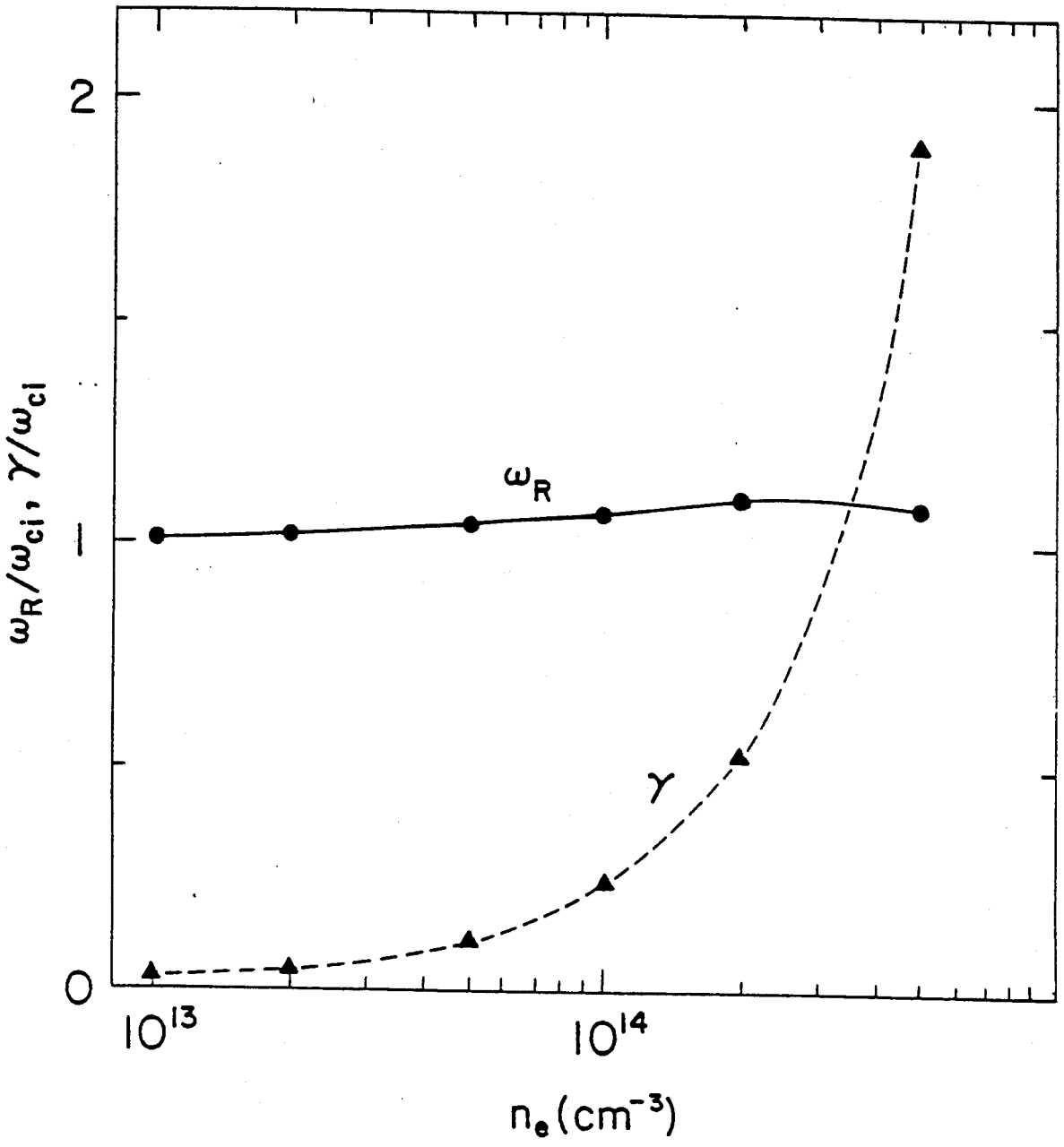
2
1
0
ω_R/ω_{ci}, γ/ω_{ci}
ω_R
γ
10^{13}
10^{14}
$n_e(cm^{-3})$

Fig. 2

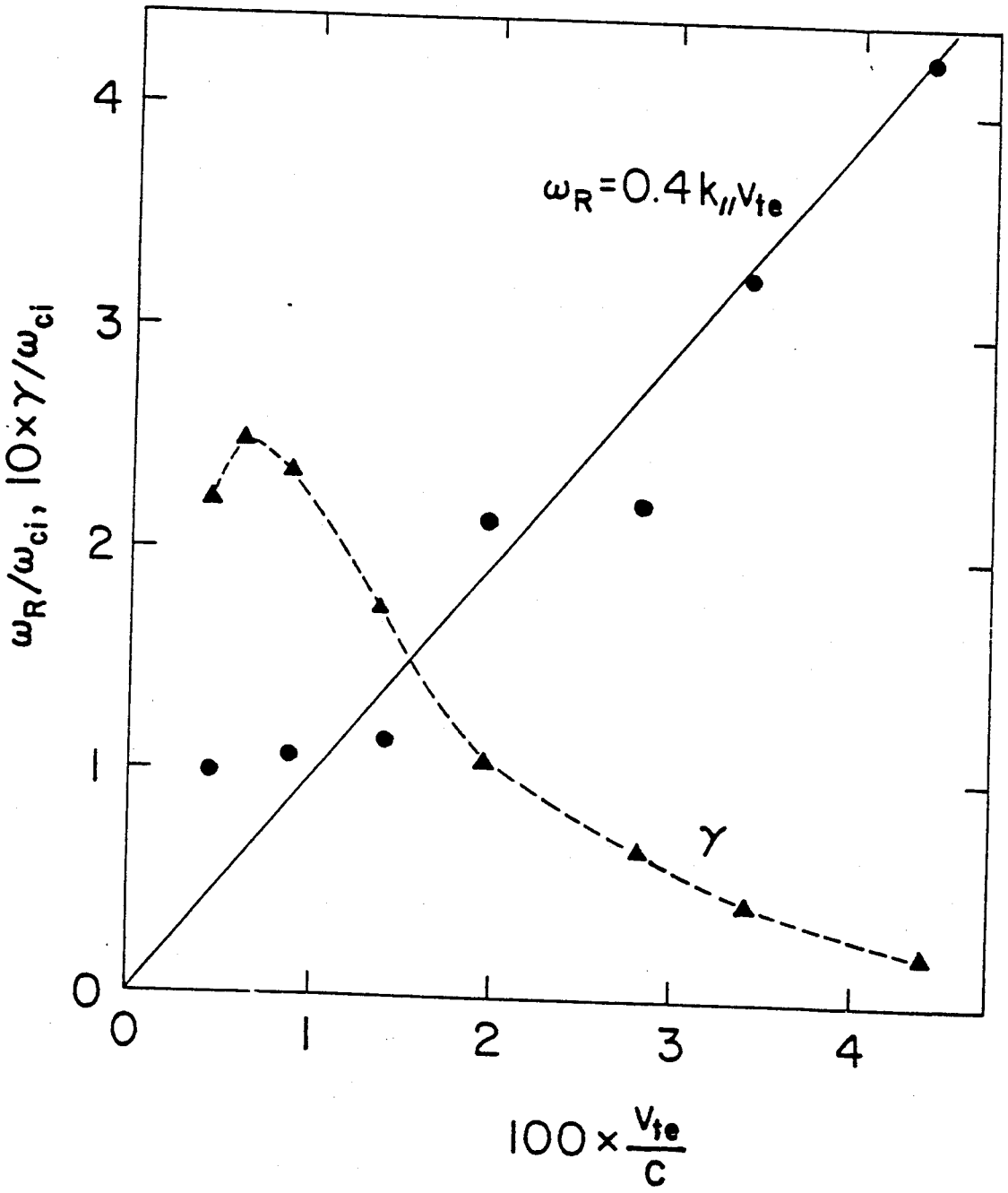
$\omega_R = 0.4\, k_{//} v_{te}$
γ
ω_R/ω_{ci}, $10\times\gamma/\omega_{ci}$
$100\times\frac{v_{te}}{c}$
0
1
2
3
4

Fig. 3

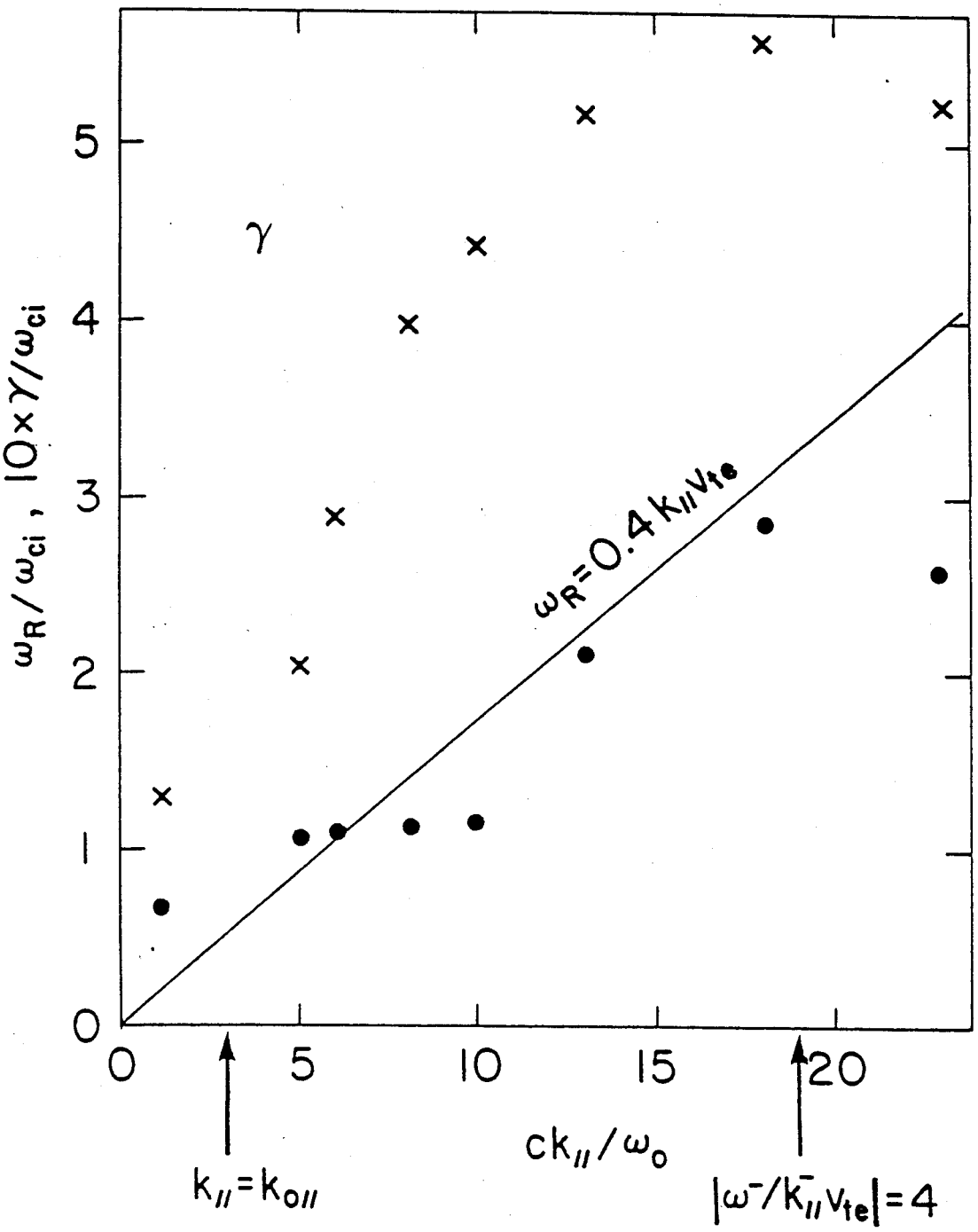
ω_R/ω_{ci} , $10\times\gamma/\omega_{ci}$
γ
$\omega_R=0.4\,k_{//}v_{te}$
$ck_{//}/\omega_o$
$k_{//}=k_{o//}$
$|\omega^-/k_{//}v_{te}|=4$
0
5
10
15
20
1
2
3
4

Fig. 4

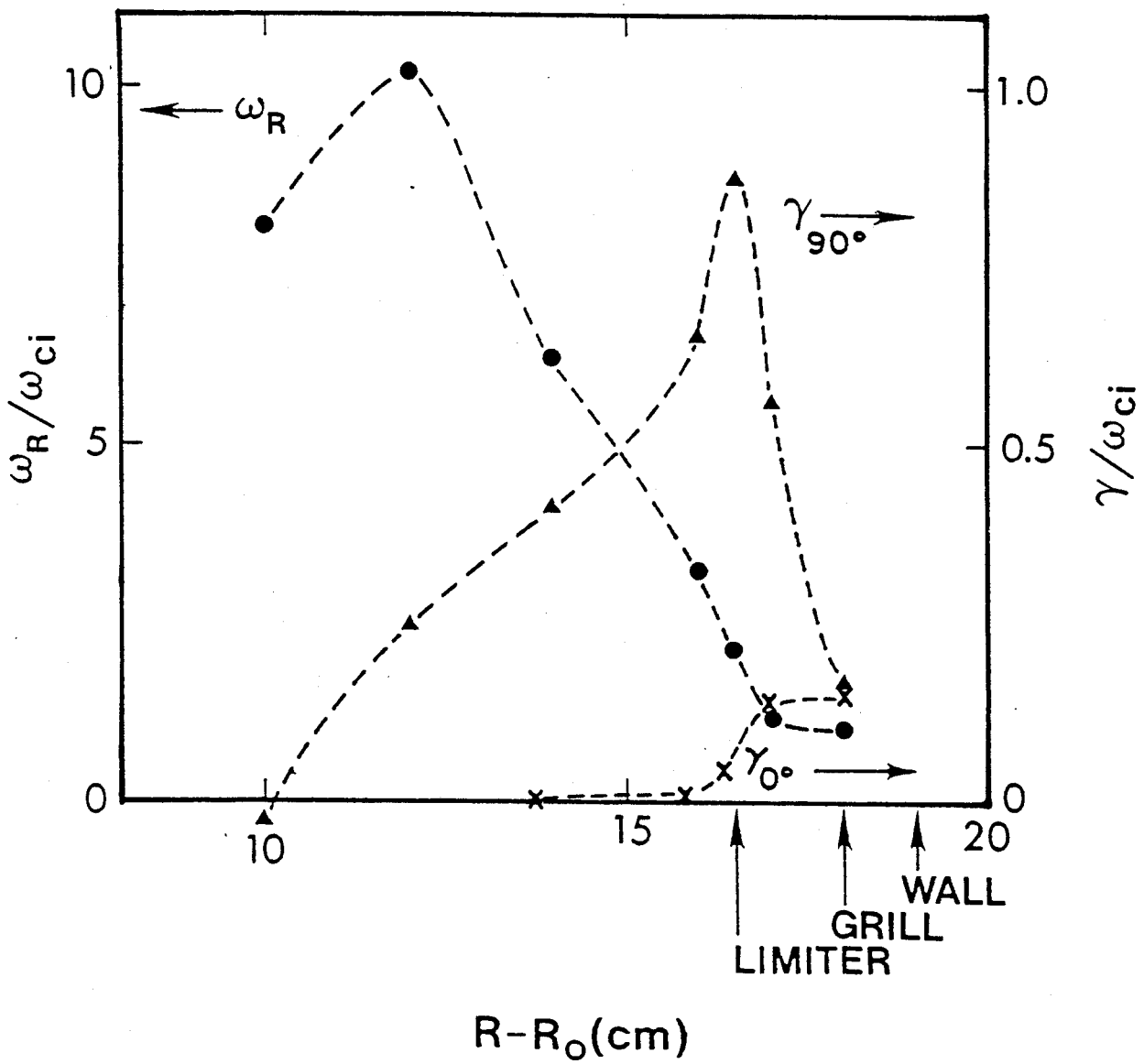
10
5
0
ω_R/ω_{ci}
$\leftarrow \omega_R$
$\gamma_{90°}$
$\gamma_{0°}$
1.0
0.5
0
γ/ω_{ci}
10
15
20
WALL
GRILL
LIMITER
$R-R_o(cm)$

Fig. 5

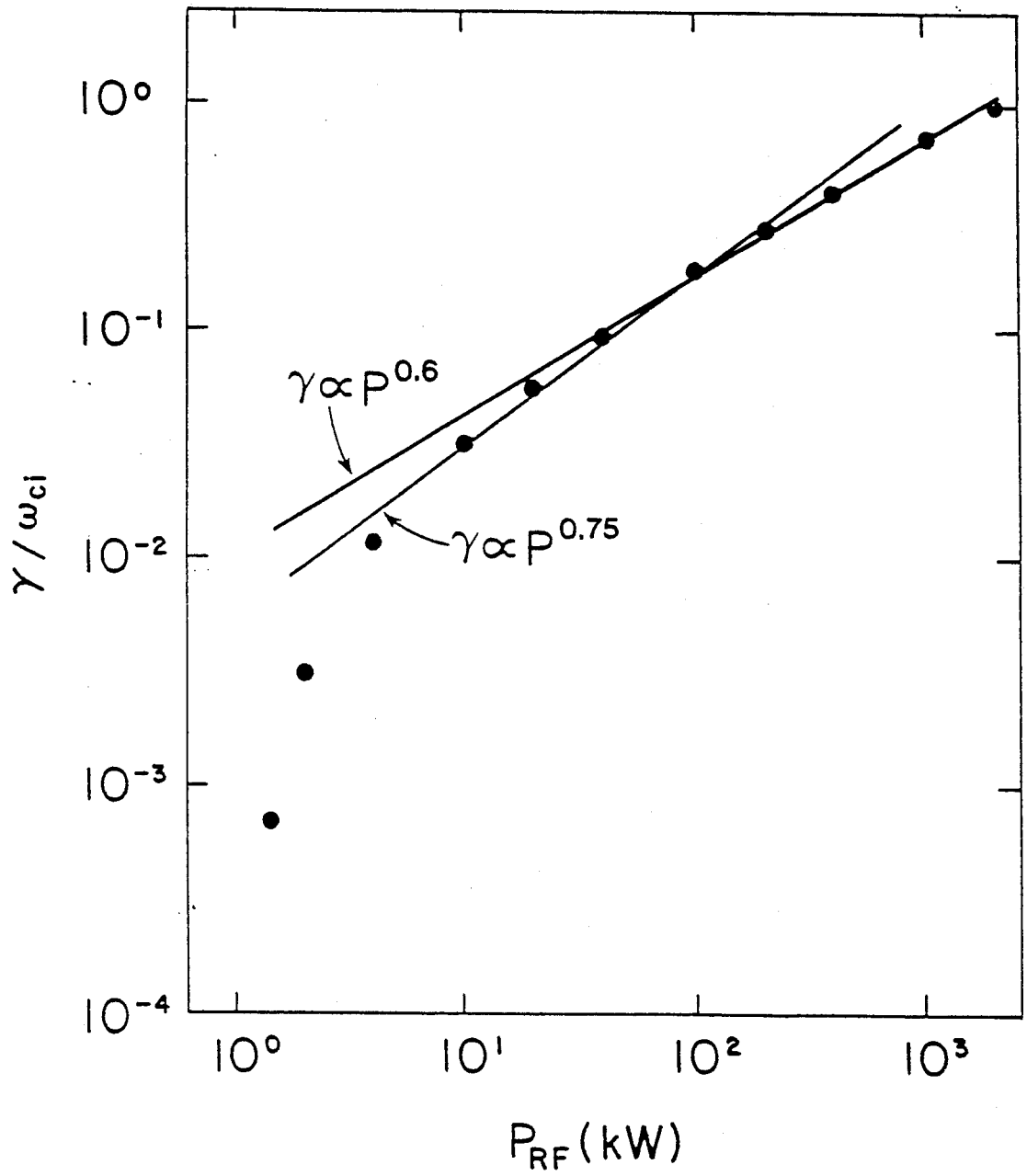
10^0
10^{-1}
10^{-2}
10^{-3}
10^{-4}
γ / ω_{ci}
$\gamma \propto P^{0.6}$
$\gamma \propto P^{0.75}$
10^0
10^1
10^2
10^3
P_{RF} (kW)

Fig. 6

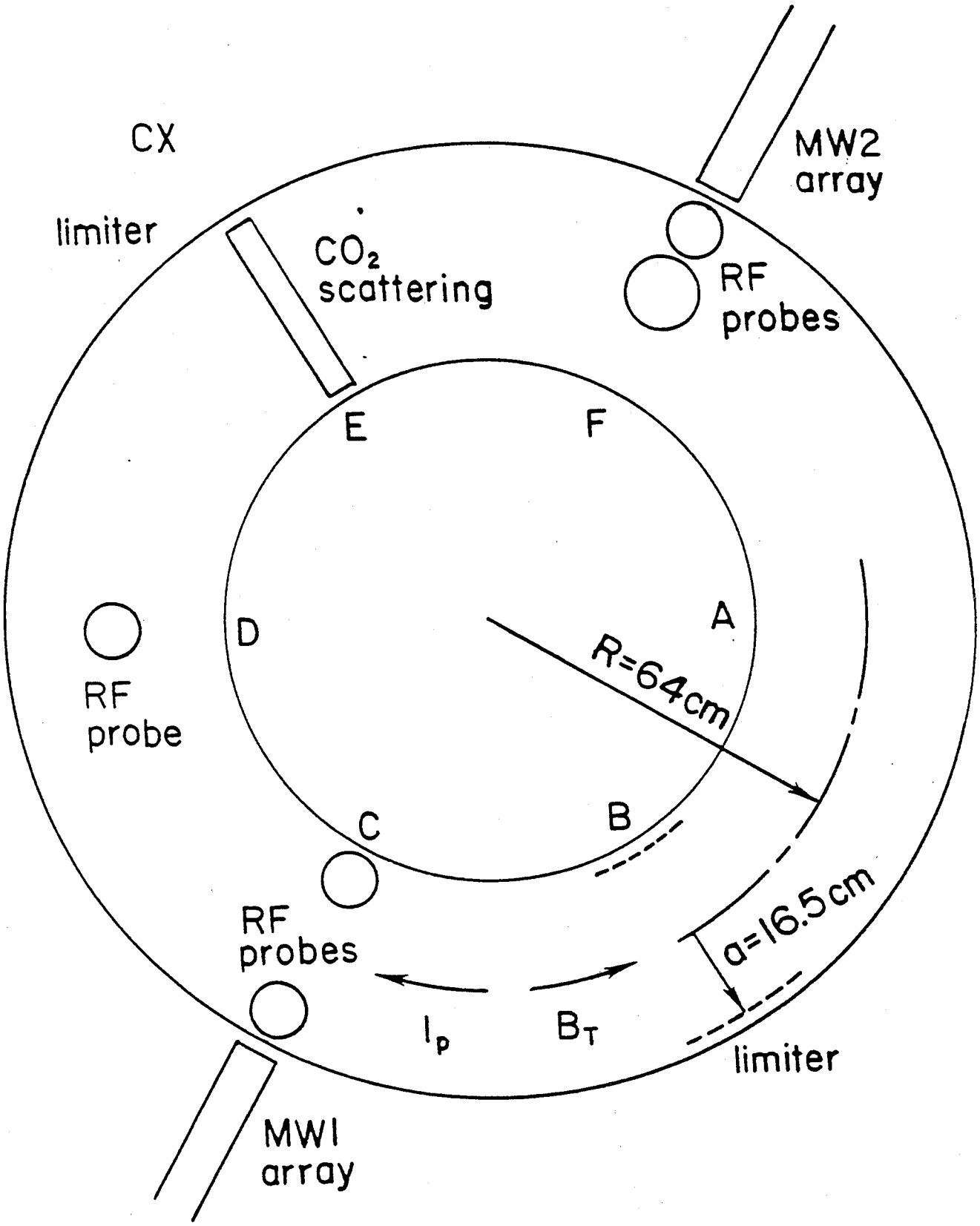
CX
limiter
MW2
array
CO_2
scattering
RF
probes
E
F
D
A
R=64cm
RF
probe
C
B
RF
probes
a=16.5cm
I_p
B_T
limiter
MWI
array

Fig. 7

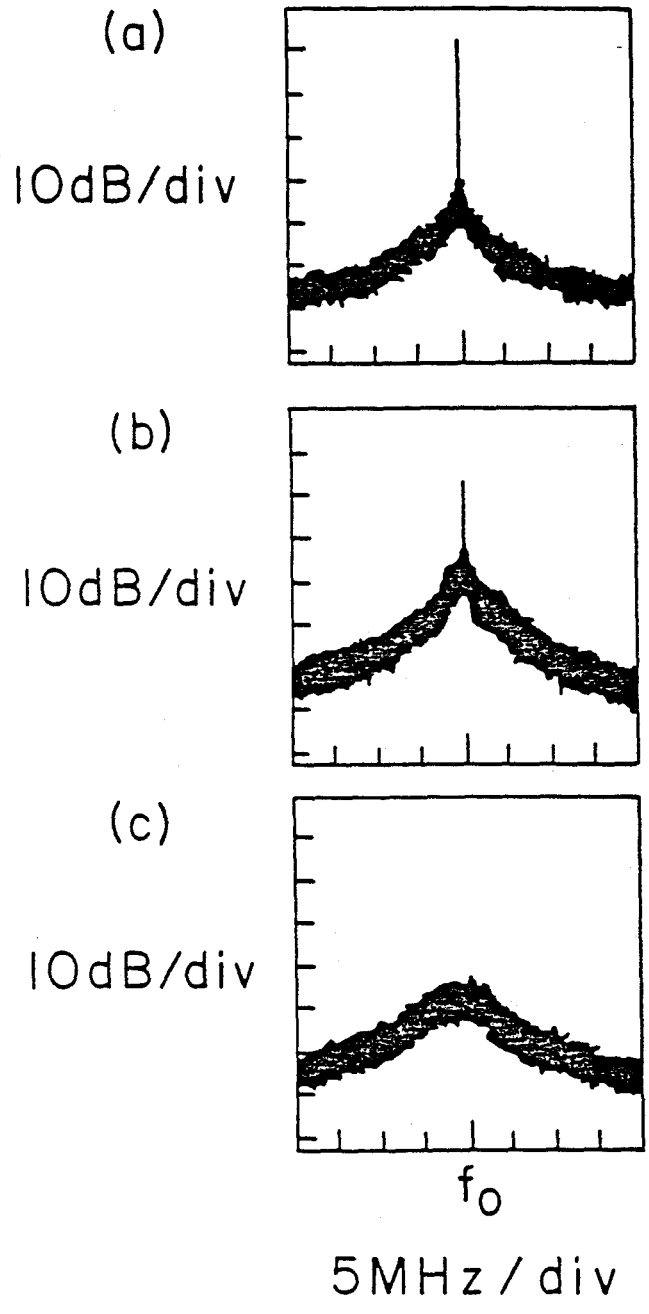

Fig. 8

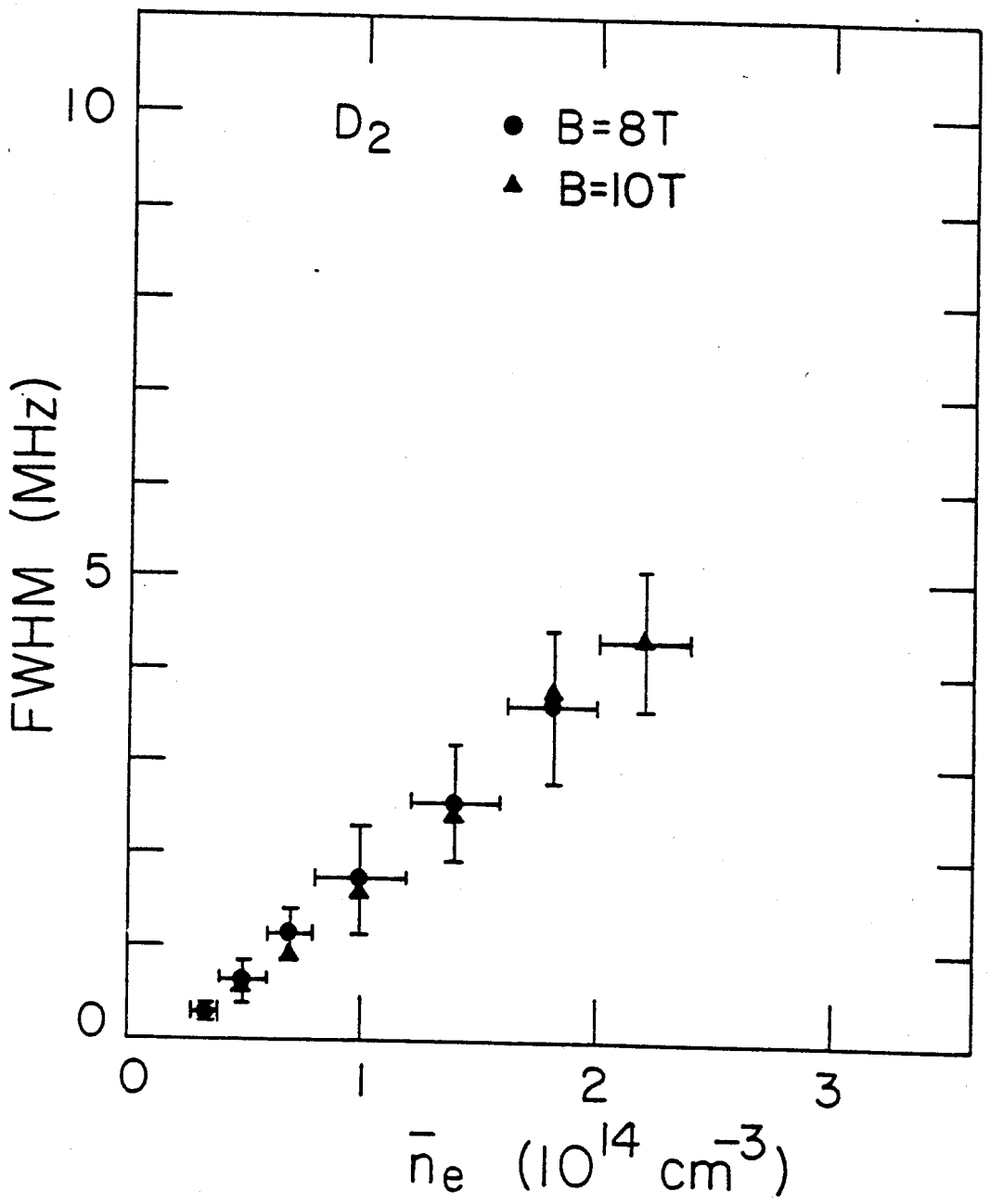

Fig. 9(a)

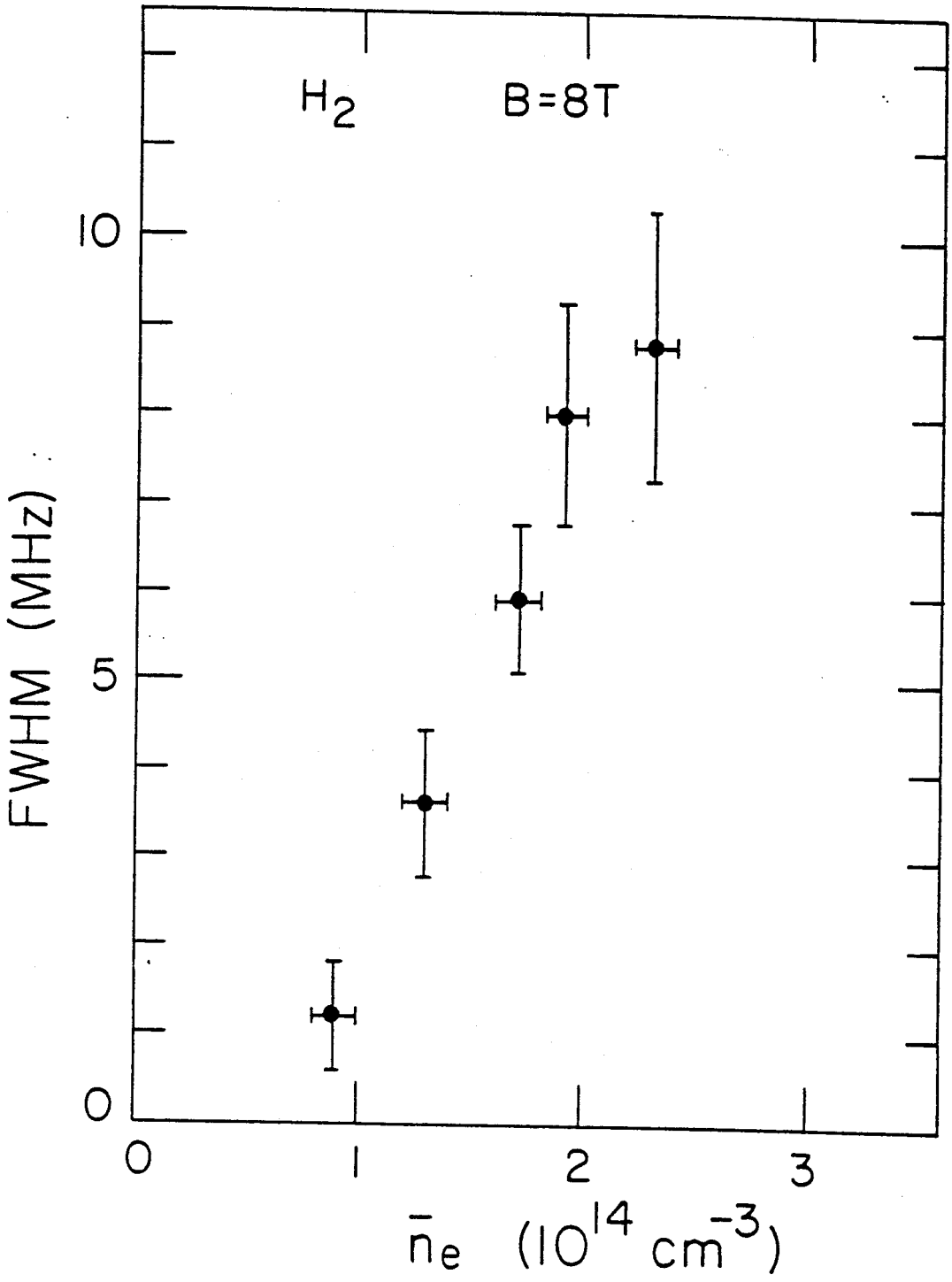

Fig. 9(b)

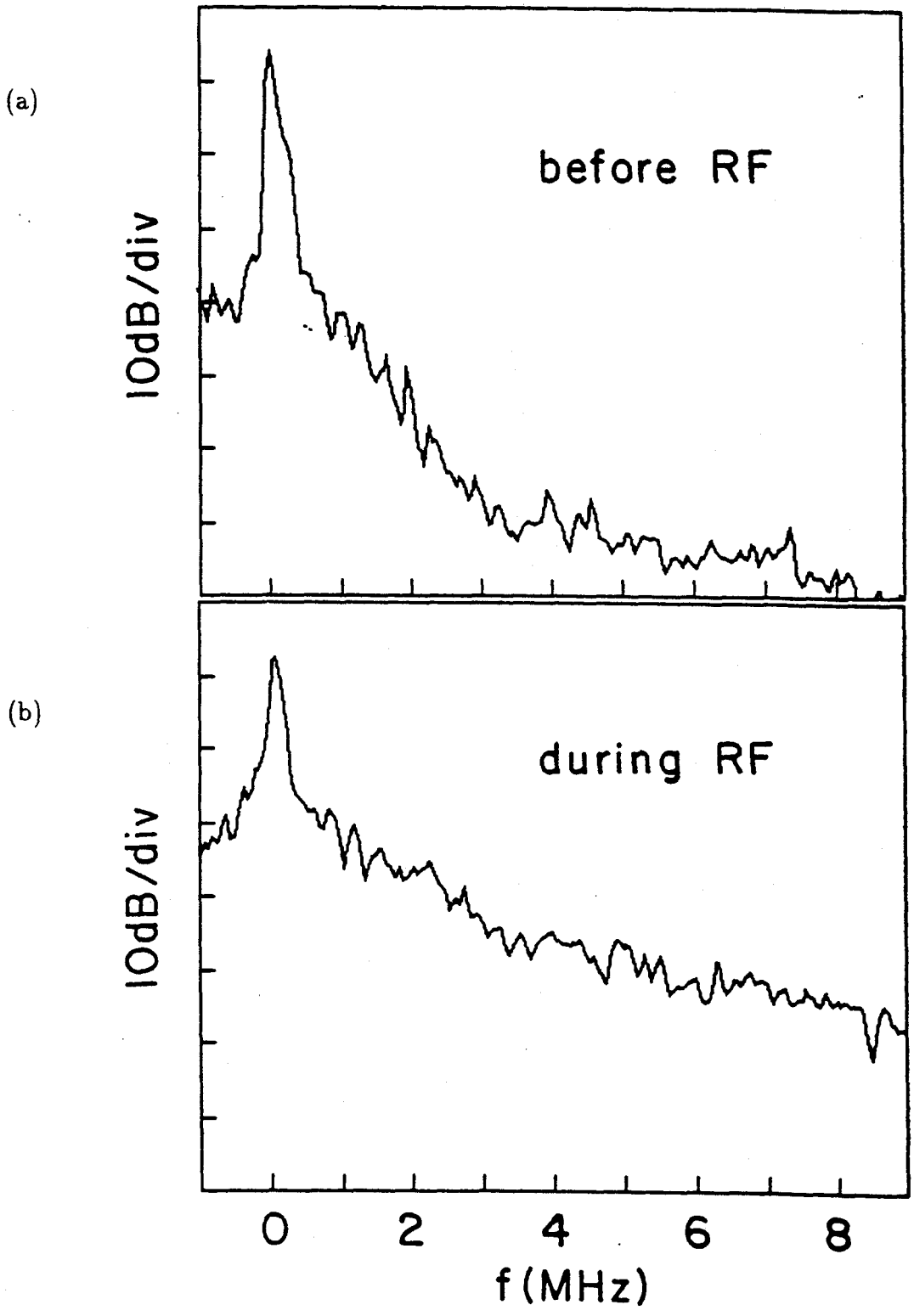

Fig. 10

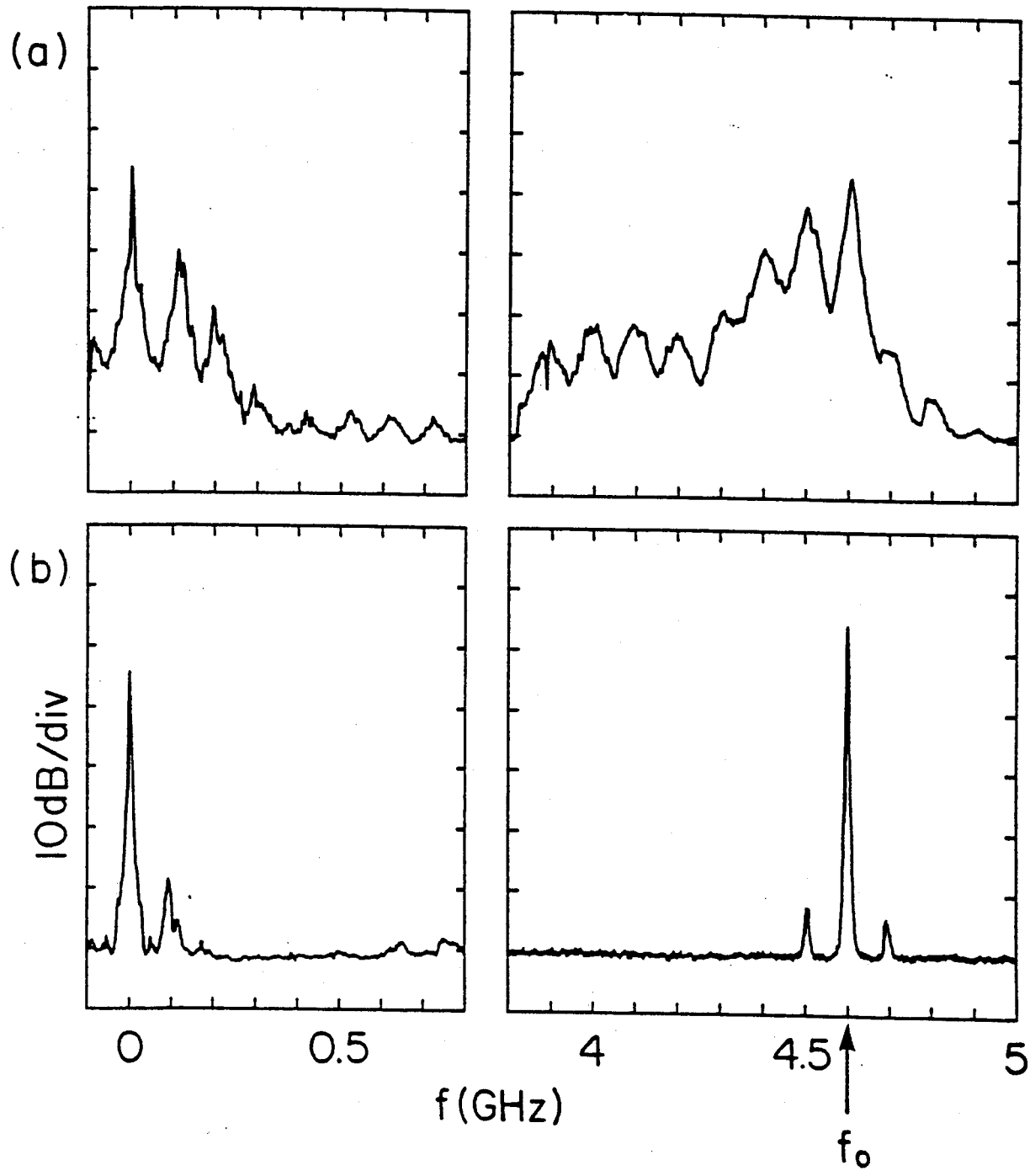

Fig. 11

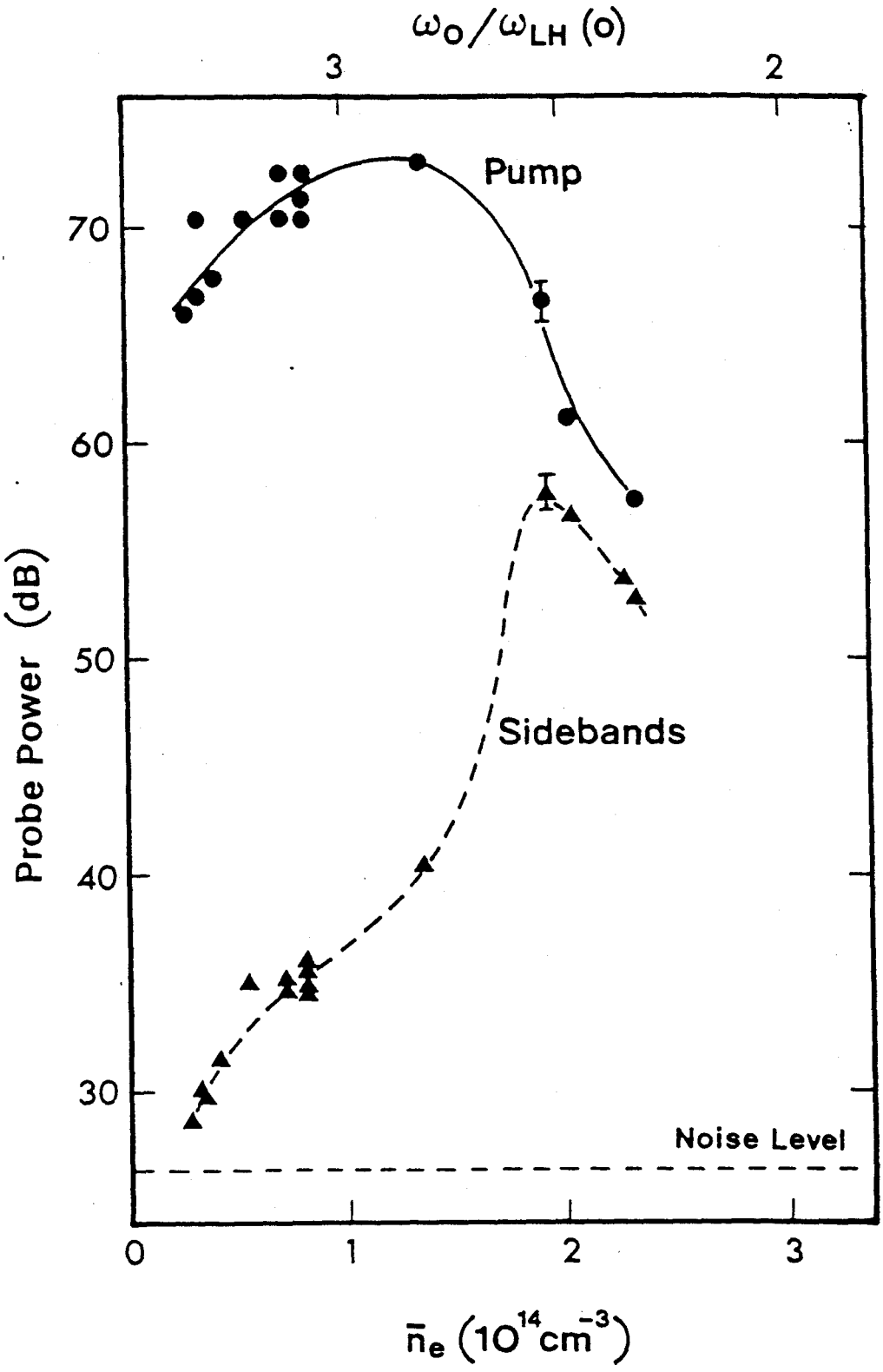
ω_o/ω_{LH} (o)
3
2
Pump
70
60
50
40
30
Probe Power (dB)
Sidebands
Noise Level
0
1
2
3
$\bar{n}_e$ (10^{14}cm^{-3})

Fig. 12

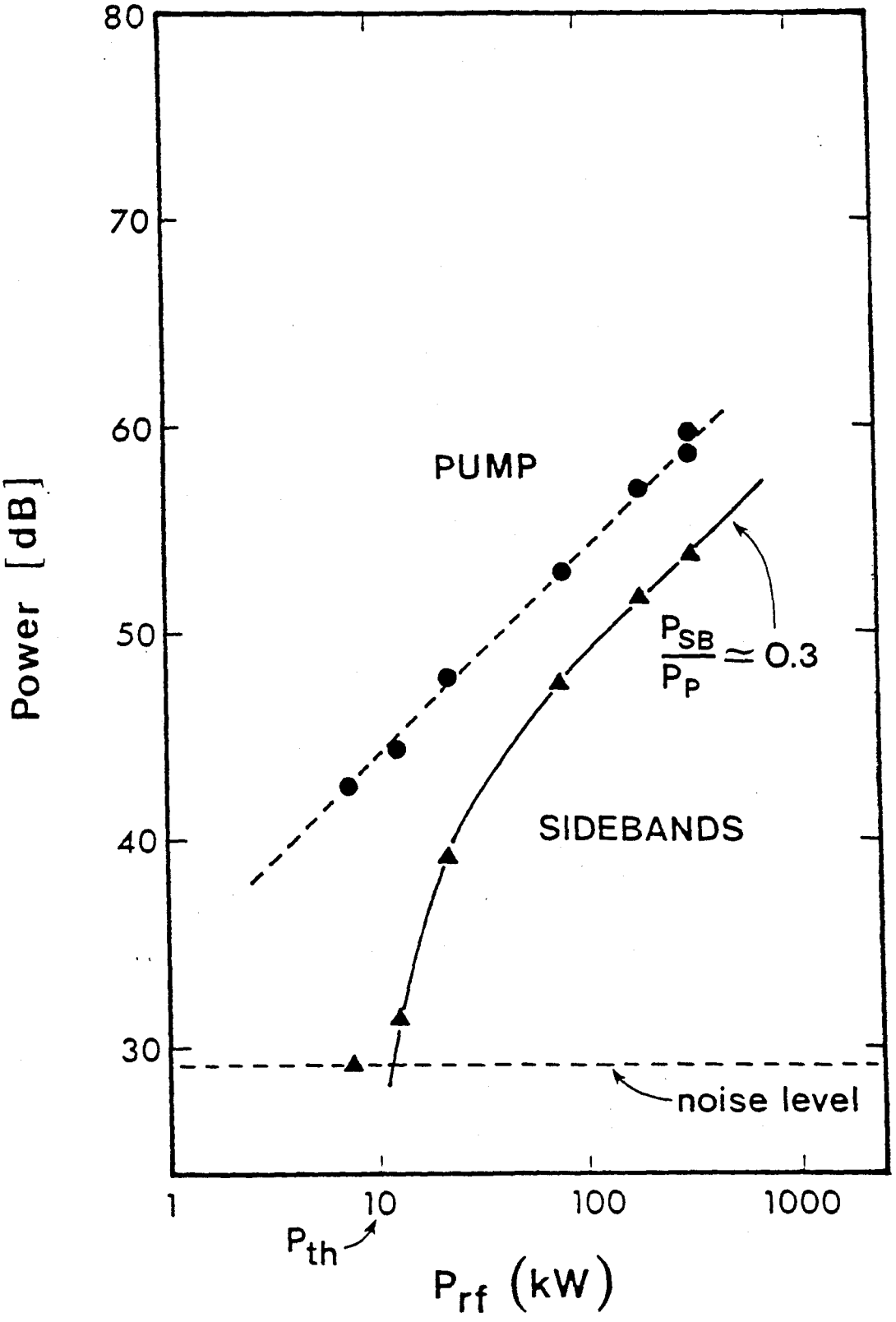
80
70
60
50
40
30
Power [dB]
PUMP
SIDEBANDS
$\frac{P_{SB}}{P_P} \simeq 0.3$
noise level
1
10
100
1000
P_{th}
P_{rf} (kW)

Fig. 13

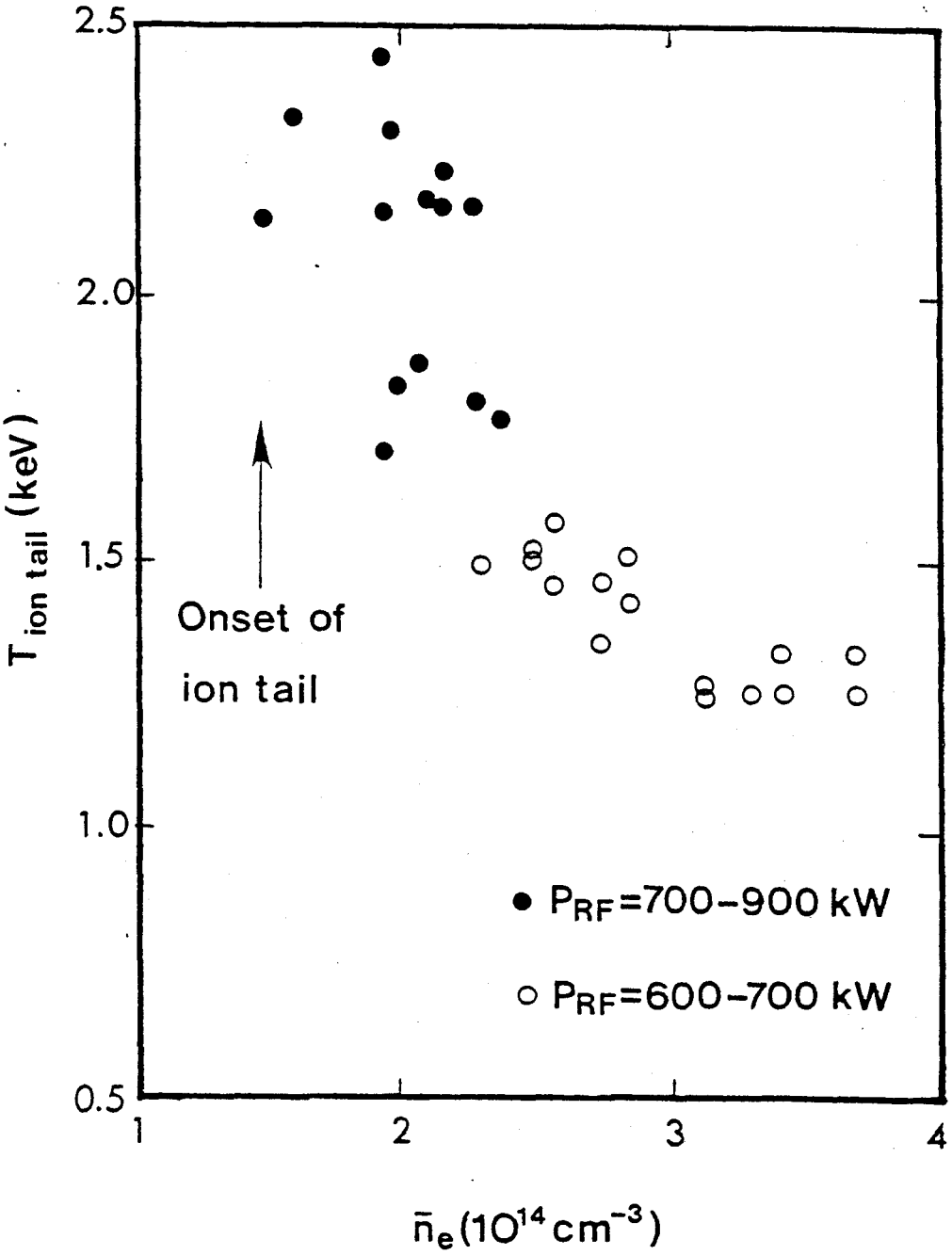
2.5
2.0
1.5
1.0
0.5
1
2
3
4
$T_{ion\ tail}$ (keV)
$\bar{n}_e(10^{14}\,cm^{-3})$
Onset of
ion tail
● P_{RF}=700–900 kW
○ P_{RF}=600–700 kW

Fig. 14(a)

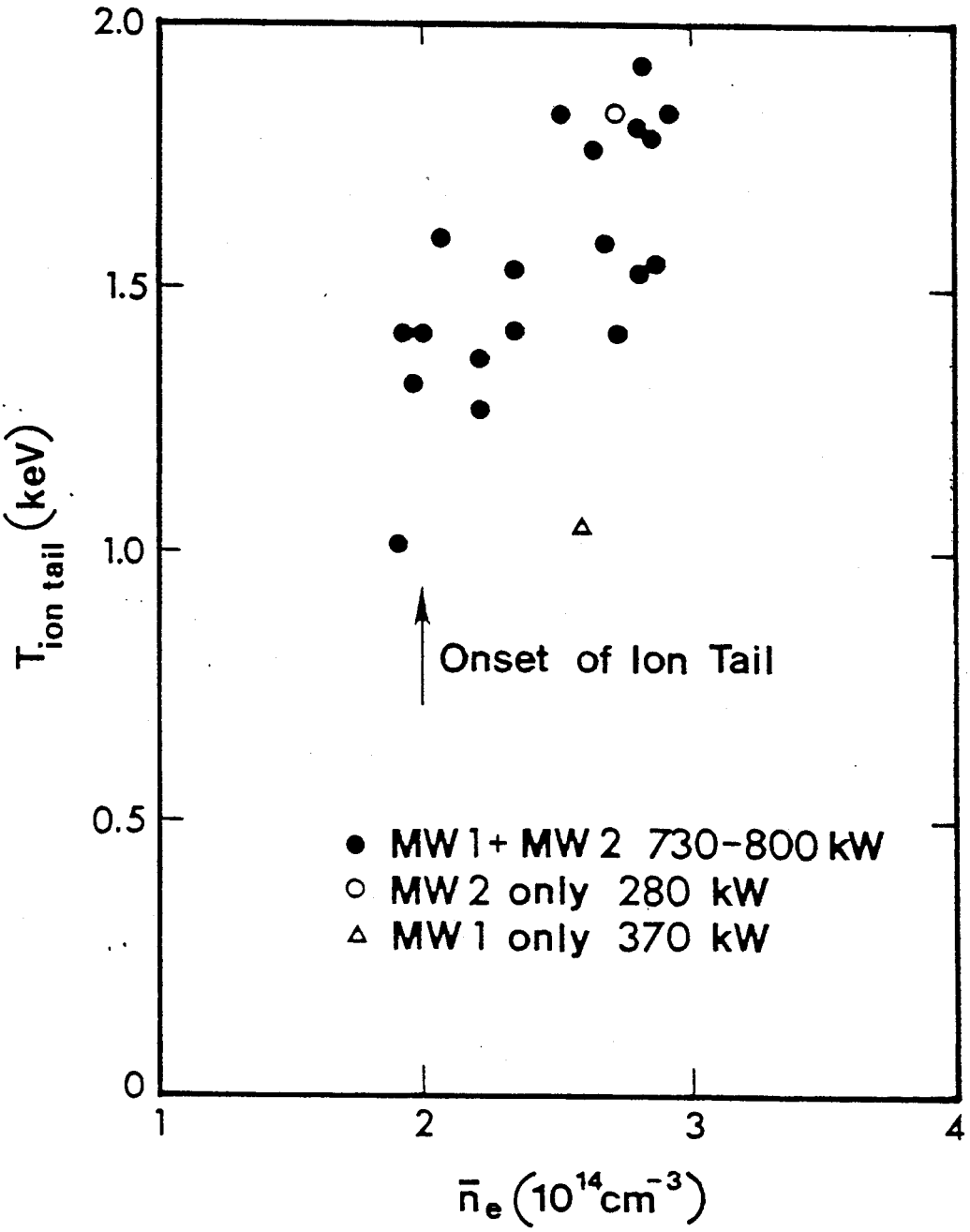
2.0
1.5
1.0
0.5
0
1
2
3
4
$T_{ion\ tail}$ (keV)
$\bar{n}_e$ (10^{14}cm^{-3})
Onset of Ion Tail
MW 1+ MW 2 730-800 kW
MW 2 only 280 kW
MW 1 only 370 kW

Fig. 14(b)

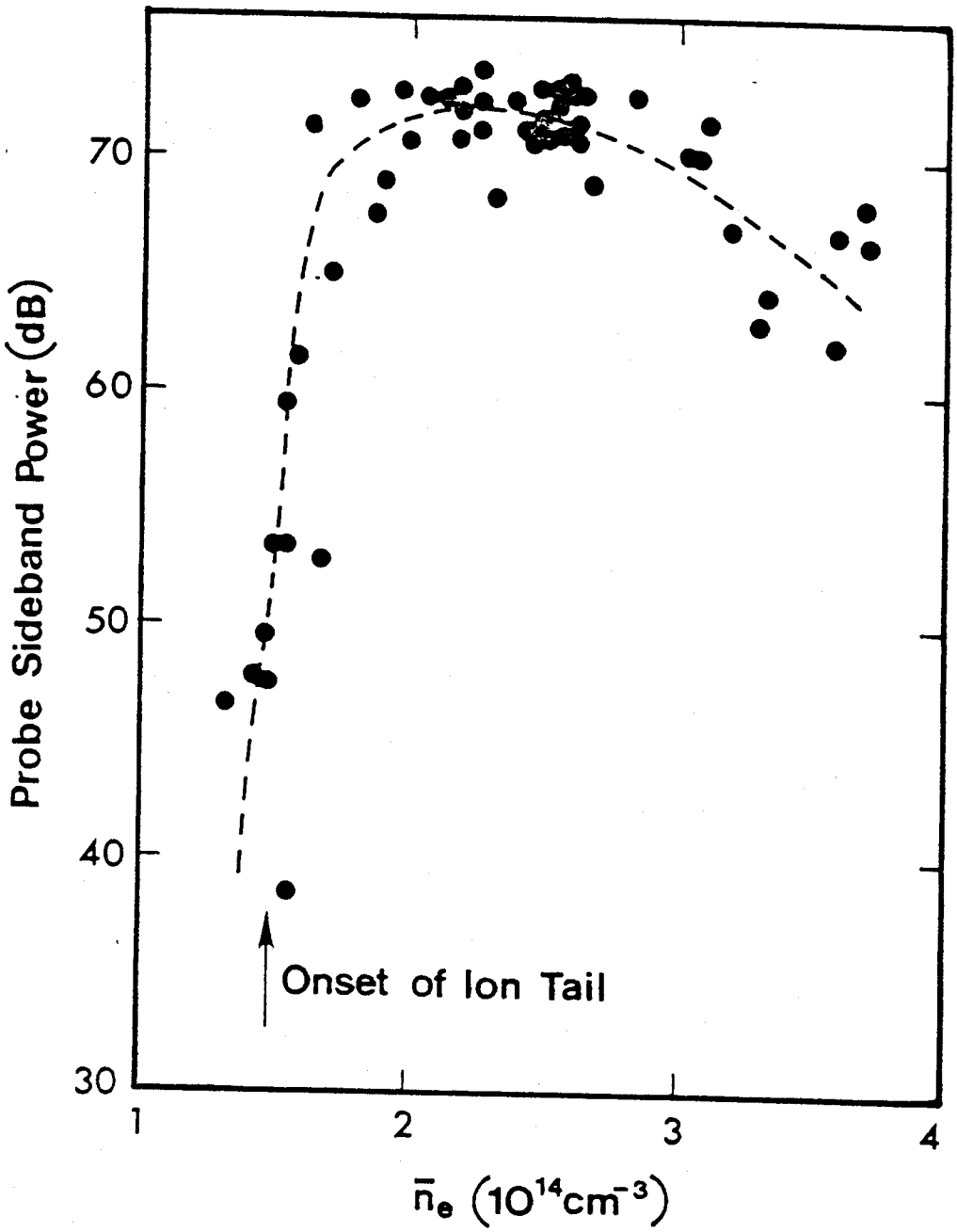
Probe Sideband Power (dB)
70
60
50
40
30
1
2
3
4
Onset of Ion Tail
$\bar{n}_e$ (10^{14}cm^{-3})

Fig. 15(a)

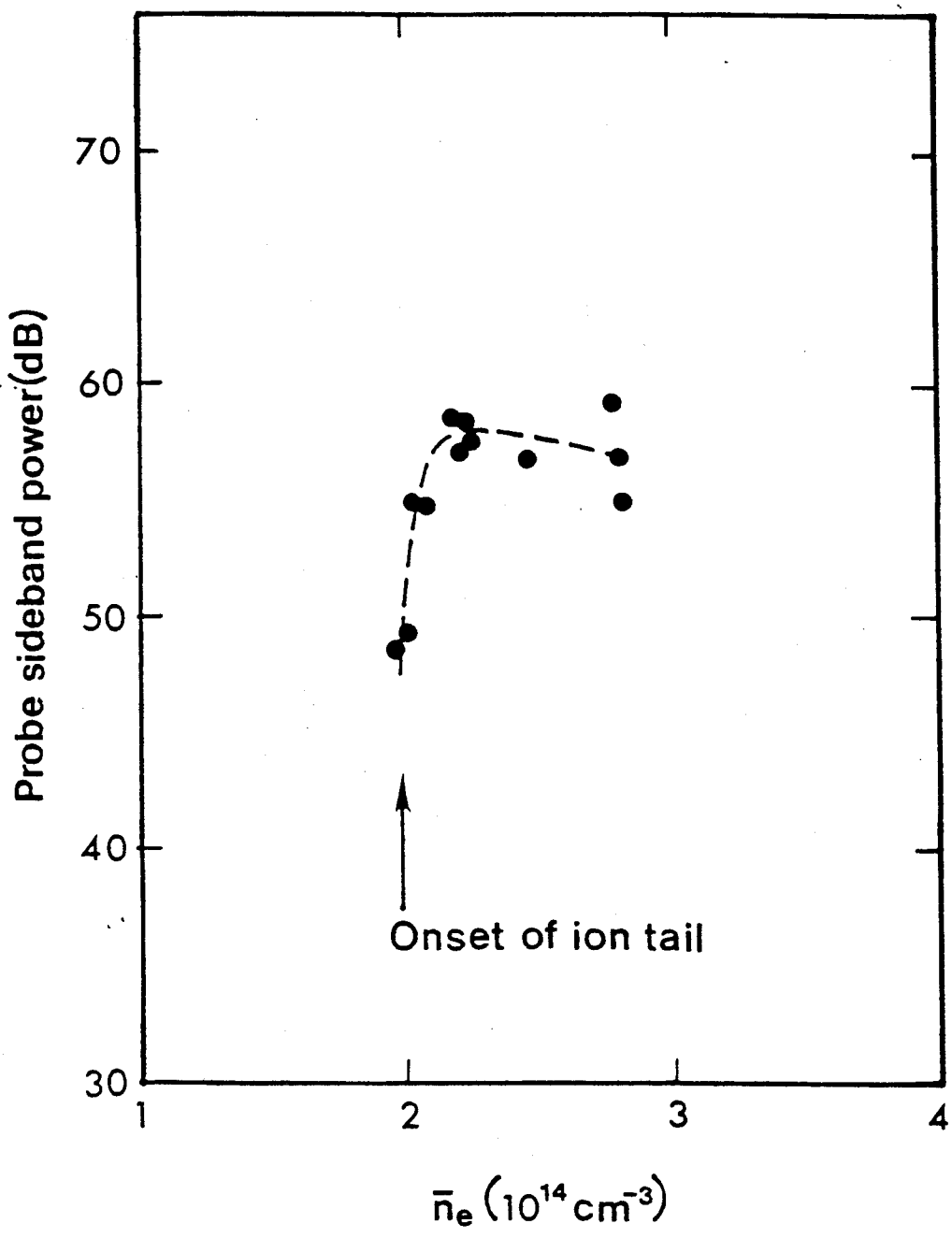
Probe sideband power(dB)
70
60
50
40
30
1
2
3
4
Onset of ion tail
$\bar{n}_e$ (10^{14} cm^{-3})

Fig. 15(b)

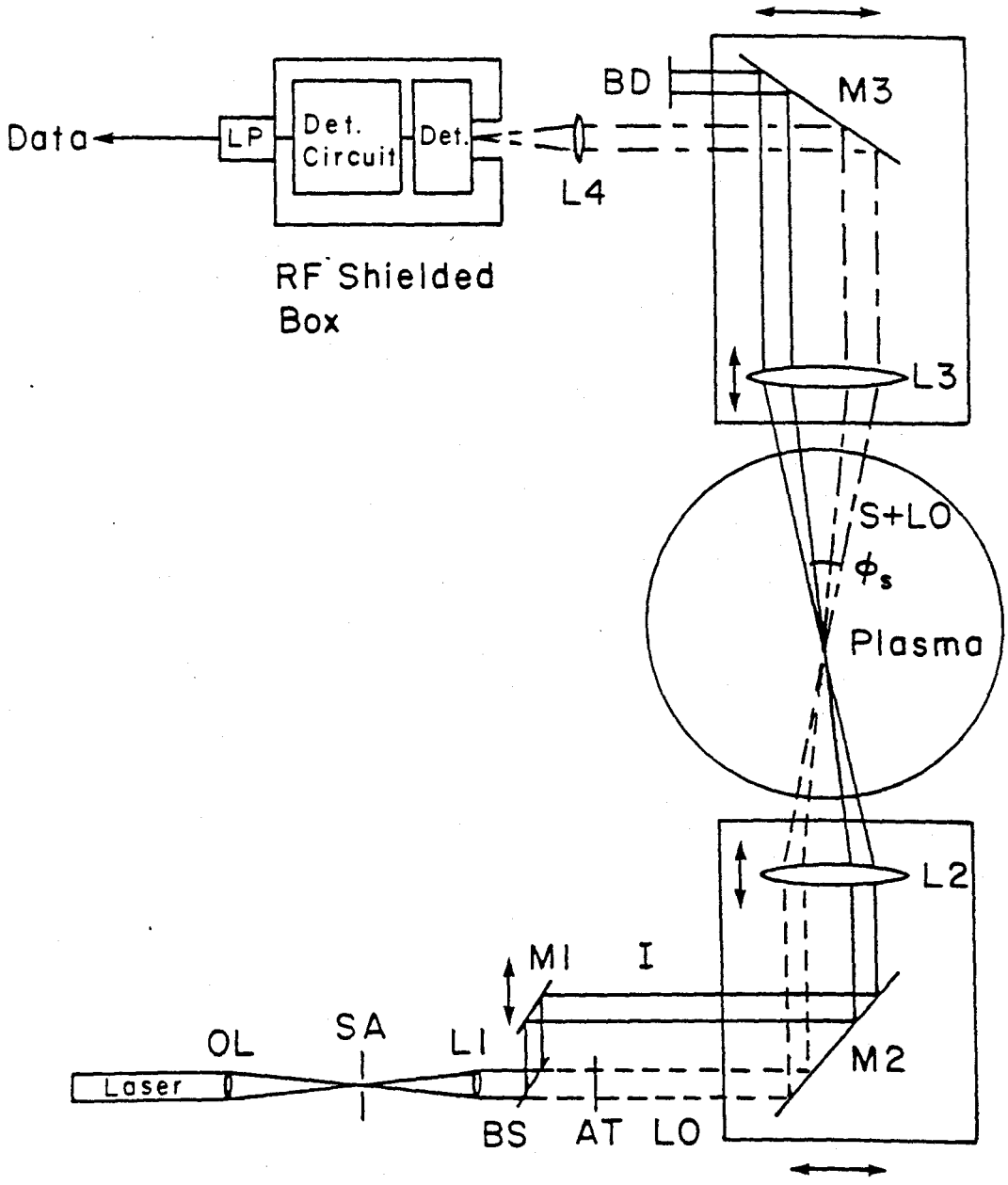
Data
LP
Det. Circuit
Det.
RF Shielded Box
L4
BD
M3
L3
S+LO
ϕ_s
Plasma
L2
MI
I
M2
OL
SA
LI
Laser
BS
AT
LO

Fig. 16

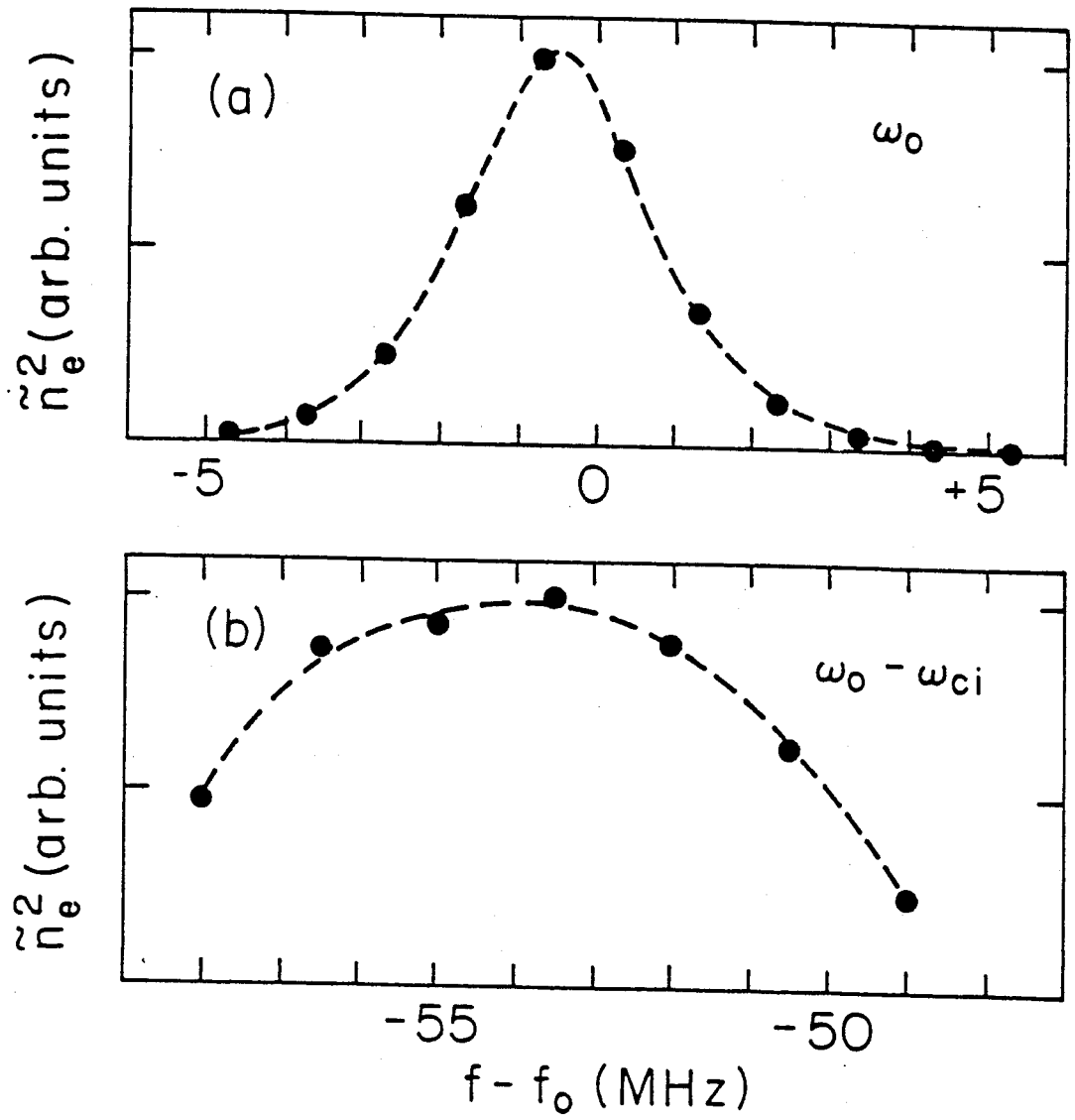
(a)
ω_o
$\tilde{n}_e^2$ (arb. units)
-5
0
+5
(b)
$\omega_o - \omega_{ci}$
$\tilde{n}_e^2$ (arb. units)
-55
-50
f - f_o (MHz)

Fig. 17

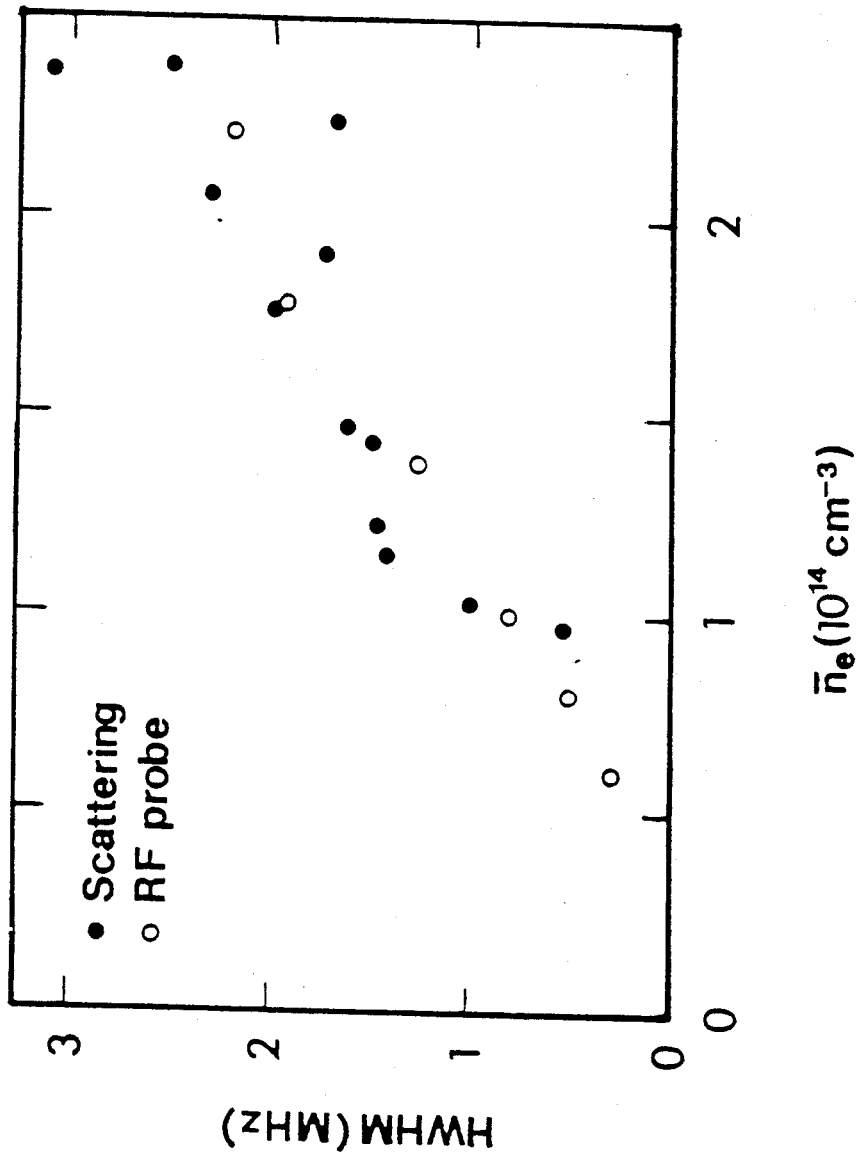

Fig. 18

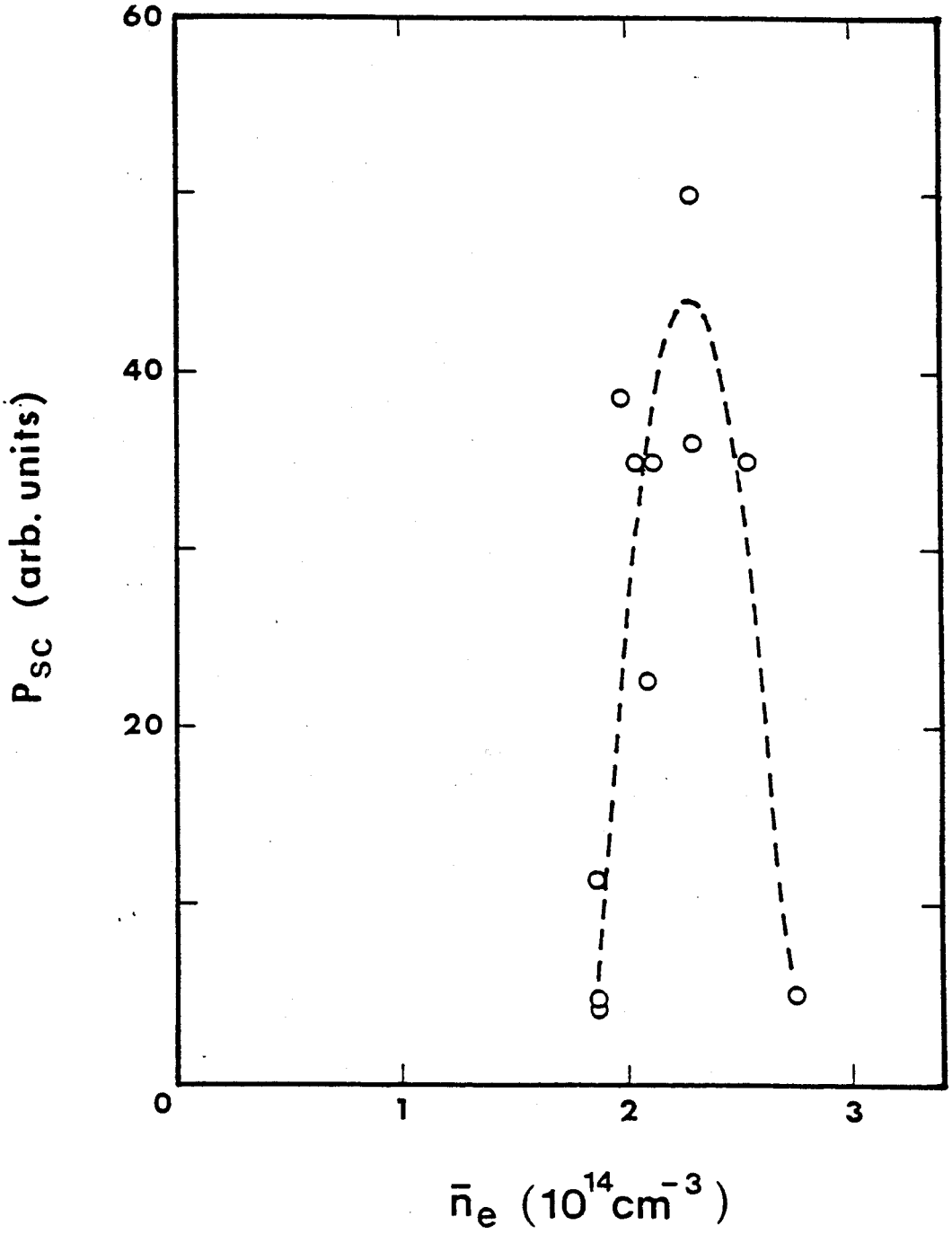

Fig. 19

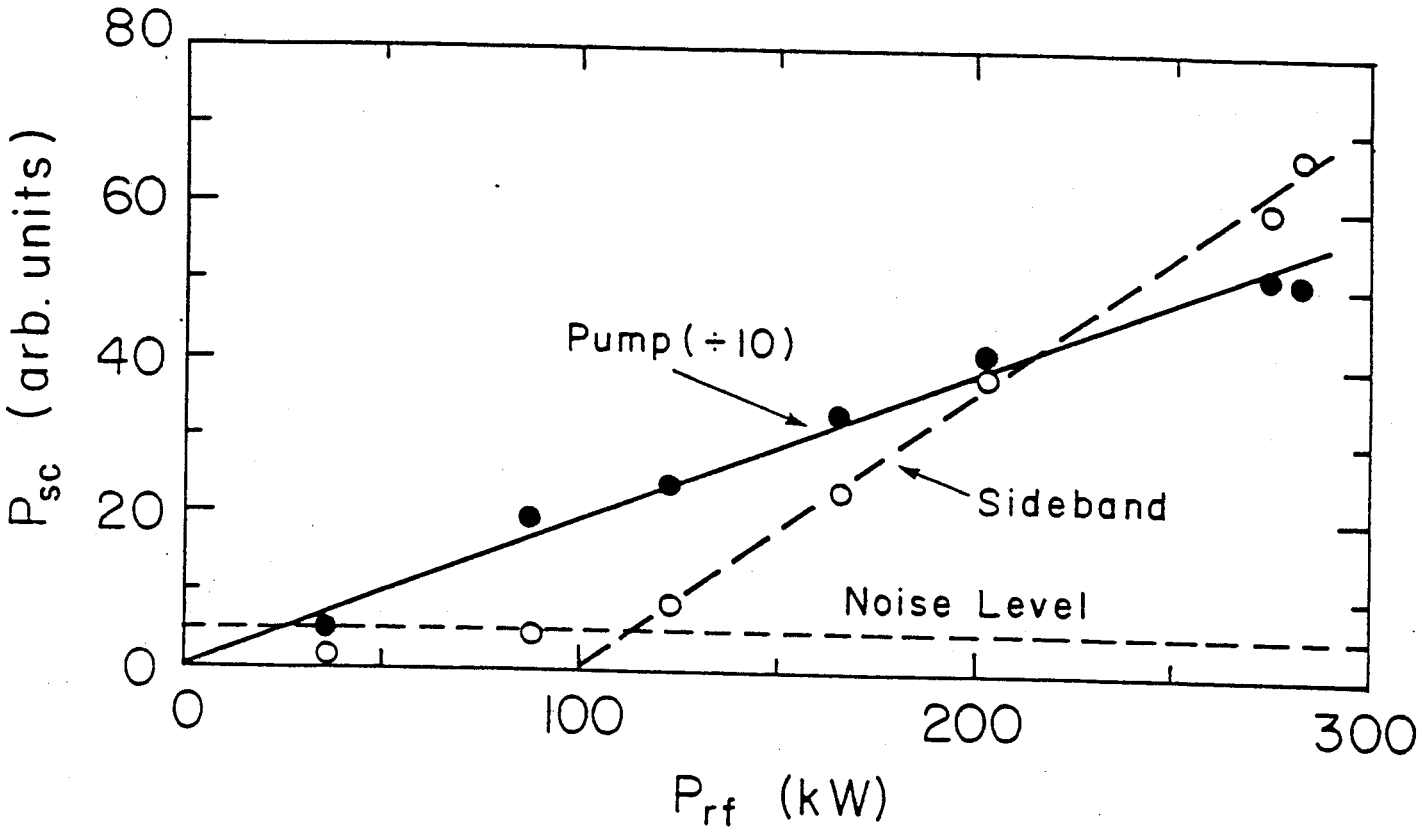
80
60
40
20
0
P_{sc} (arb. units)
Pump (÷10)
Sideband
Noise Level
0
100
200
300
P_{rf} (kW)

Fig. 20

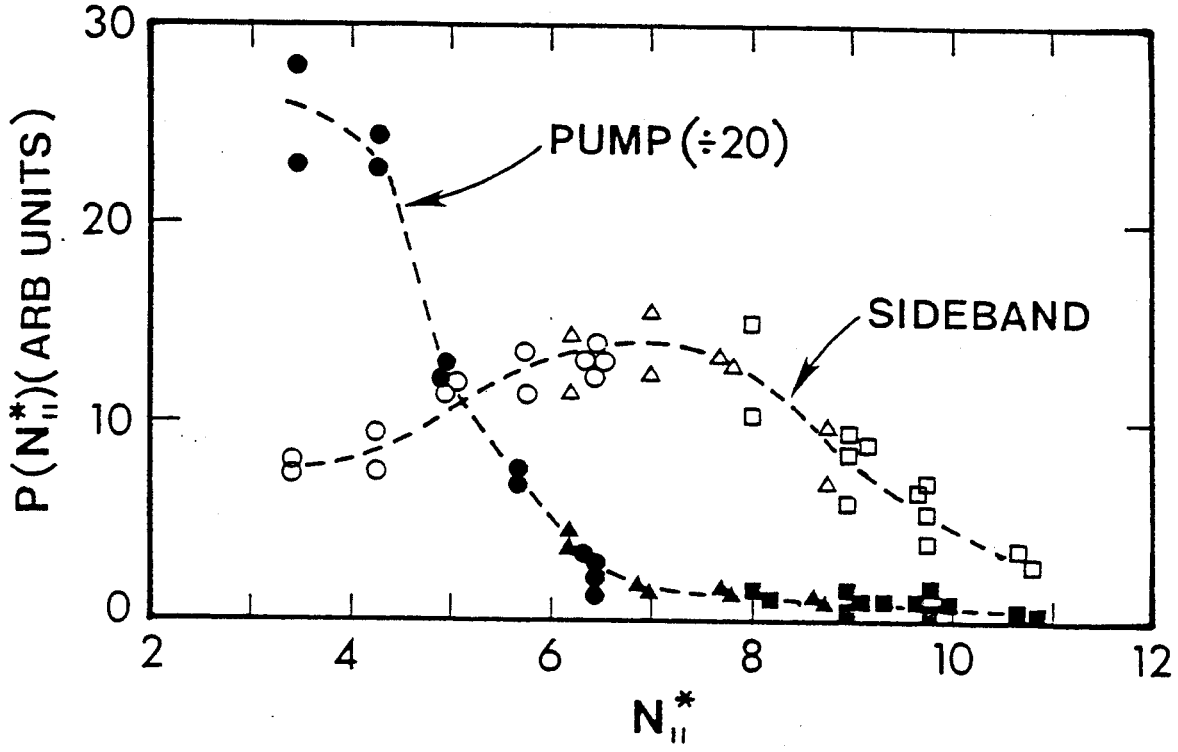

Fig. 21